S22 Advanced Topics in Optics
Tópicos Avanzados en Óptica
13/07 Wednesday afternoon, Aula 1.1

15:30-15:45 Jesús Armengol Cebrian (Universidad Politécnica de Cataluña)
Optical and visual quality indicators of intraocular lenses measured with an on-bench eye model

15:45-16:00 Verónica González Fernández (Universidad Complutense de Madrid)
Comparative study of enhanced monofocal lenses for different nominal powers

16:00-16:15 Sonia Ortiz Peregrina (Universidad de Granada)
Effects of smoking cannabis on visual performance

16:15-16:30 Miriam Casares López (Universidad de Granada)
The influence of visual function on driving performance under the influence of alcohol

16:30-16:45 Vahid Pourreza Ghoushchi (Universidad de Murcia)
Periodic blur fluctuations effect on contrast sensitivity

16:45-17:00 Alberto de Castro Arribas (IO-CSIC, Madrid)
Personalized computational models with OCT. Challenges and opportunities

17:00-18:00 **Posters and Coffee**

18:00-18:15 Rosa María Martínez Ojeda (Universidad de Murcia)
Enhanced second harmonic imaging of the living human eye using deconvolution

18:15-18:30 Luis Ordóñez Angamarca (Universidad Jaime I)
Optical sectioning in microscopy with structured illumination and single pixel detection

18:30-18:45 Manuel Martinez Corral (Universidad de Valencia)
Advances in Fourier Lightfield Microscopy

18:45-19:00 Víctor Bernardo Puente (Hamamatsu Photonics France)
Quantum imaging with a photon number resolving camera

19:00-19:15 Jose Manuel Crespo Contiñas (Universidad de Santiago de Compostela)
Computer generated training datasets for deep learning applications to ESPI fringe patterns

19:15-19:30 Ana Jesús López Díaz (Universidad de La Coruña)
Desarrollo de un sistema de procesado láser 3D asistido por robot para la eliminación de pintura

Posters:

43 E. Josua Fernandez Martinez (Universidad de Murcia)
Manipulating the second order coherence function for super-resolution intensity correlation imaging

44 Laura Clavé Cerezo (Universidad Politécnica de Cataluña)
Visual acuity in phakic and monofocal pseudophakic eyes under red, green, and blue lights

45 Justo Arines Piferrer (Universidad de Santiago de Compostela)
Jacobi Fourier Polynomials: more flexibility for designing ophthalmic solutions

46 Juan Manuel Bueno García (Universidad de Murcia)
Optical coherence tomography in retinitis pigmentosa patients treated with an injection of autologous bone-marrow-derived mononuclear stem cells

47 Diego Montagud-Martínez (Universidad Politécnica de Valencia)
Caracterización cromática de una lente intraocular comercial de foco extendido

48 Anabel Martínez Espert (Universidad de Valencia)
Impacto de la aberración esférica en modelos de ojos teóricos

49 Aina Turull Mallofré (Universidad Politécnica de Cataluña)
Analysis of the accommodation response as a supporting tool during subjective refraction

50 Alba María Paniagua Diaz (Universidad de Murcia)
Visual simulation and correction using economic and compact vertical aligned liquid crystal devices

51 Dulce María Simón Badia (Universidad de Murcia)
Straylight and Optical Memory Effect characterization of ex-vivo cataractous crystalline lenses

52 Pedro Gil (Universidad de Murcia)
Effects of small residual astigmatism on the reading performance of contact lens neophytes

53 Adriana Rosalía Sánchez Montes (Universidad de Alicante)
Numerical analysis of cross-talk phenomena in pixelated PA-LCos devices

54 Joan Josep Sirvent Verdú (Universidad de Alicante)
Precise-Integration Time-Domain for Optical Anisotropic Media

55 Iryna Standret (Universidad de Murcia)
Investigating ergodicity for the determination of optical coherence functions

56 Pien Vinke (Universidad de Murcia)
Impact of the detector response on the temporal second degree of coherence of a chaotic light source

57 Erik Baradit Allendes (Universidad del Bio-Bio)
Characterization of topography hidden under paint by means of algorithms stable to the number of frames under non-uniform illumination

S22 Advanced Topics in Optics
Tópicos Avanzados en Óptica

14/07 Thursday afternoon, Aula 1.1

15:30-15:45 Esther Nabadda (Universidad Miguel Hernández)
Synchronous phase detection technique for the evaluation of complex functions displayed on a phase-only modulator

15:45-16:00 María del Mar Sánchez López ((Universidad Miguel Hernández)
Proof-of-concept depolarization emulator based on a liquid-crystal spatial light modulator

16:00-16:15 Tomás Lloret López (Universidad de Alicante)
Quality metrics in holographic lenses recorded in a low toxicity photopolymer

16:15-16:30 José Carlos García Vázquez (Universidad de Alicante)
Reflection gratings stored in a nanoparticle-doped photopolymer

16:30-16:45 José Carlos Mira Martínez (Universidad de Alicante)
Redes plasmónicas unidimensionales de nanopartículas de oro a partir de redes de relieve fabricadas holográficamente

16:45-17:00 Víctor Bonal Díaz (Universidad de Alicante)
Latest advances in organic distributed feedback lasers with top-layer resonators

17:00-18:00 **Coffee Break**

Two lines of space reserved to include
codes of the symposium and of this communication

Optical and visual quality indicators of intraocular lenses measured with an on-bench eye model

Jesús Armengol*, Fidel Vega, María Sagrario Millán

Department of Optics and Optometry, Violinista Vellsolà 37 08222 Terrassa, Spain.

*e-mail: jesus.armengol@upc.edu

Cataract surgery is evolving from a solution to overcome visual impairment to a refractive procedure thanks to the development of intraocular lenses (IOLs) that are better adapted to the visual demands of the patients. Nowadays, there is a myriad of new IOL designs on the market, with associated claims from the manufacturers, that need to be carefully assessed in independent laboratories.

Optical quality indicators of IOL's performance can be measured using an eye model on an optical bench [1] avoiding subject variability. Modern extended range of vision (ERV) IOL designs aim to remedy the loss of the accommodative capacity of the natural lens with either a focal segment or by joining multiple foci (multifocal IOL). In a through-focus analysis of the IOL, the optical imaging quality of the lens is evaluated around the main focus of the eye model (typically corresponding to far vision).

An eye model implemented on a test bench (Figure 1) according to the standard regulation [1] allowed us to assess a variety of commercial IOLs and to extract some optical and visual quality indicators. A more detailed description of the setup is found in Ref. [2].

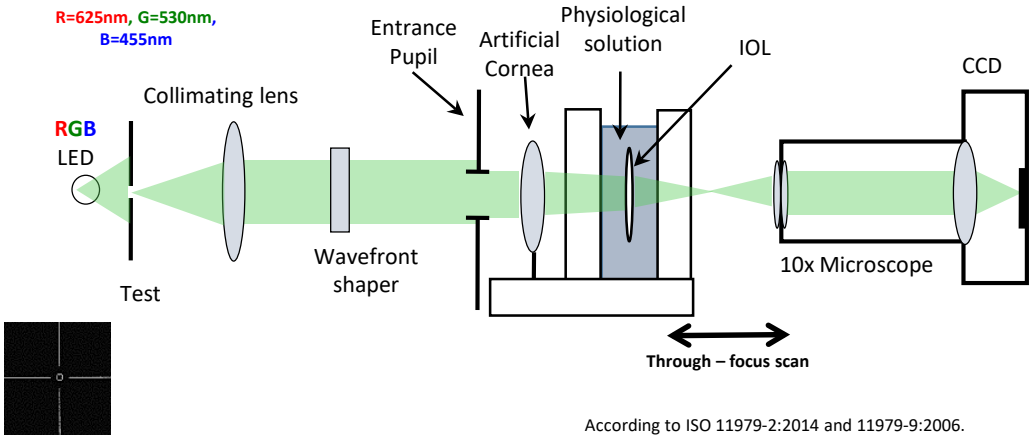

Figure 1. Sketch of the optical setup with an eye model. Test used to obtain the LSF (bottom left).

From the measurement of the line spread function (LSF), the modulation transfer function (MTF) was computed and, further, an optical quality indicator named the Strehl ratio of the radial MTF (SRMTF) (Eq.1) and a visual quality indicator named the visual Strehl ratio (VSMTF) (Eq.2).

$$SRMTF = \frac{\int_0^\infty MTF_r df}{\int_0^\infty MTF_{r\_DL} df} \qquad (1) \qquad VSMTF = \frac{\int_0^\infty CSF_n * MTF_r \, df}{\int_0^\infty CSF_n * MTF_{r\_DL} \, df} \qquad (2)$$

In Eq. 1, MTFr stands for radial MTF and subscript DL accounts for diffraction-limited calculation. In Eq. 2, CSFn stands for the neural contrast sensitivity function that represents the neural response of the visual system [3]. In this work we present the through-focus SRMTF and VSMTF results obtained experimentally for a commercial trifocal IOL (Zeiss ATLISA_Tri839MP) and compare between them. The impact of a constant magnification approach along the through-focus range is discussed.

[1] ISO 11979-2:2014 and 11979-9:2006. *"Ophthalmic Implants - Intraocular Lenses" Geneva.*
[2] F. Vega, F. Alba-Bueno, and M. S. Millán, *J. Eur. Opt. Soc. Rapid Publ.* **9**, 14002 (2014).
[3] L. N. Thibos, X. Hong, A. Bradley, and R. A. Applegate, *J. Vis.* **4**(4), 329 (2004).

Funding: Ministerio de Ciencia e Innovación, Agencia Estatal de Investigación (PID2020-114582RB-I00/ AEI / 10.13039/501100011033).

Two lines of space reserved to include
codes of the symposium and of this communication

Comparative study of enhanced monofocal lenses for different nominal powers

Verónica González-Fernández[1,*], Nuria Garzón[2], María García-Montero[2], César Albarrán Diego[3], Luis Miguel Sánchez-Brea[1], José Antonio Gómez-Pedrero[1]

[1]Dpto. de Óptica, Universidad Complutense de Madrid, Av. Arcos del Jalon 118, E-28037 Madrid, Spain. [2]Dpto. de Optometría y Visión, Universidad Complutense de Madrid, Av. Arcos del Jalon 118, E-28037 Madrid, Spain. [3]Dpto. de Óptica, Optometría y Visión, Universitat de València, Doctor Moliner 50 46100 Burjassot, Spain.

*e-mail: veronicagf@ucm.es

Among the wide range of intraocular lenses (IOLs), monofocal lenses are one of the most common options due to its simplicity. Nevertheless, they present obvious limitations for which different solutions are being designed. One of these solutions, are the called "enhanced" monofocal lenses that improve intermediate vision, without reaching the criteria for extended range lenses. These new designs seek to increases the depth of focus to improve the intermediate vision, without modifying far vision and reducing dysphotopsia.

One of the approaches modifies the spherical aberration in a limited quantity to not compromise the optical quality of the final image. Therefore, the total addition of the lens will be limited. Of course, the different strategies or modifications will lead to different optical performances.

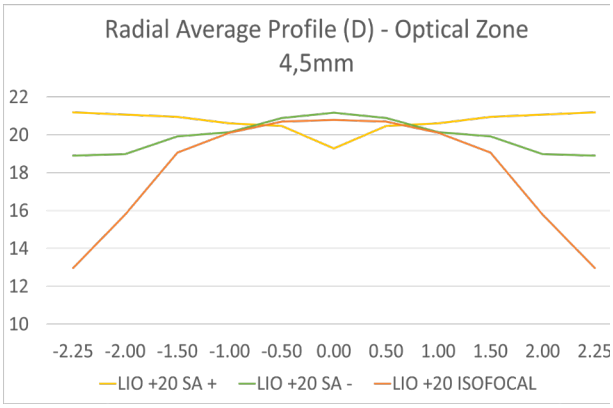

Figure 1. Comparison of the radial average profile for three enhanced monofocal lenses with a nominal power of +20 D: isofocal (orange), with positive spherical aberration (yellow) and negative spherical aberration (green).

In this work, we present the comparative study of three different lenses with the same nominal power: +20.00 D, measured using an optical system based on a quantitative deflectometry technique that measures light deviations through a combination of the Schlieren principle with a phase-shifting method (NIMO TR1504). All lenses were measured in a balanced salt solution at different aperture diameters. The three lenses differ in the sign and amount of spherical aberration induced to enhance intermediate vision. The optical lens power distribution as a function of the aperture radius was described in terms of radial computed colour maps, radial averaged power profiles, spherical aberration, and aberrometric profiles for difference distances from centre.

The power profiles of the lenses analysed showed that the enhanced monofocal lens nominal power did not change from the centre to the periphery, contrary to the enhanced ones that revealed a change toward more positive power values from the centre to the periphery (see Fig. 1). The refractive power of the enhanced monofocal lenses did not reach the value of the nominal distance power (+20.00D) until a radial distance of between -0.5 and +0.50 mm from the centre of the lens.

Acknowledgements: The authors thank Ministerio de Economía y Competitividad for the project PID2019-105918GB-I00.

Effects of smoking cannabis on visual performance

Sonia Ortiz-Peregrina*, Carolina Ortiz, Miriam Casares-López, Pilar Granados-Delgado, José R. Jiménez, Rosario G Anera

Department of Optics, University of Granada, Campus Fuentenueva s/n CP 18071, Granada (Spain)

*e-mail: soniaortiz@ugr.es

Introduction: Cannabis constitute the most widely consumed illicit drug worldwide [1, 2]. Moreover, its consumption is expected to increase due to the legalization in several countries [3]. The main psychoactive compound of cannabis is the so called Δ9-tetrahydrocannabinol (THC) and it is able to bind to the cannabinoid receptors, some of them are present within the visual system [4, 5]. However, visual effects of cannabis consumption remains unknown.

Objective: This study aimed to investigate visual effects of smoking cannabis in several visual functions, and its relationship with visual effects perceived by the user.

Methods: The study was prospectively approved by the University of Granada Human Research Ethics Committee (921/CCEIH/2019). Thirty-one young occasional cannabis users were included in the study. Visual function was evaluated in two different experimental sessions: a baseline session without cannabis use and other session after smoking cannabis. Both sessions were counterbalanced, and visual function was evaluated for visual acuity, contrast sensitivity, stereopsis, accommodative response, straylight and halo perception. Participants completed a questionnaire about self-perceived visual quality under the effects of cannabis. Depending on whether or not they perceived worsening in visual quality after smoking cannabis, they were classified into two groups.

Results: Smoking cannabis significantly deteriorated vision. Visual acuity and contrast sensitivity were significantly reduced ($p<0.001$). Intraocular scattering increased about 9% after cannabis use ($p<0.001$) resulting in greater halo perception ($p=0.016$). Accommodative lag increased after smoking cannabis for 0.4 m ($p=0.006$) and 0.2 m ($p=0.001$). Stereopsis also deteriorated, with an increase of 50.7% for near distance ($p<0.001$) and 213.1% for far distance ($p<0.001$). Despite these results, about one third of the sample indicated that they think their vision is not impaired under cannabis' effect. A binary logistic regression analysis identified contrast sensitivity as the only visual test significantly associated with self-perceived visual quality (Odds ratio: 1.135; 95% CI 1.006, 1.280; $p=0.040$).

Conclusions: Smoking cannabis has negative consequences for visual function. However, some users are not aware of these changes. Contrast sensitivity is associated with the perceived impairment in visual function under cannabis effects.

[1] European Monitoring Centre for Drugs and Drug Addiction (EMCDDA). European Drug Report 2019: Trends and Developments 2019 (Publications Office of the European Union, Luxembourg, 2019).
[2] Spanish Observatory on Drugs and Addictions. Survey on alcohol and drugs in Spain (EDADES), 1995–2017 (Ministerio de Sanidad, Consumo y Bienestar social, Madrid, 2017).
[3] Compton, W. M., Volkow, N. D. & Lopez, M. F. Medical marijuana laws and cannabis use: Intersections of health and policy, *JAMA Psychiatry* **74**, 559 (2017).
[4] Dasilva, M., Grieve, K. L. & Rivadulla, C., Cannabis, endocannabinoid CB1 receptors, and the neuropathology of vision. In Neu-ropathology of Drug Addictions and Substance Misuse (ed. Preedy, V. R.) 738–748 (Elsevier, Amsterdam, 2016).
[5] Yazulla, S. Endocannabinoids in the retina: From marijuana to neuroprotection, *Prog. Retin. Eye Res*. **27**, 501 (2008).
[6] Ortiz-Peregrina, S., Ortiz, C., Casares-López, M., Jiménez J.R., Anera, R.G., Effects of cannabis on visual function and self-perceived visual quality. *Sci Rep.* **11**, 1655.

Acknowledgements: Research Projects PID2020-115184RB-I00, funded by MCIN/ AEI/10.13039/501100011033, and A-FQM-532-UGR20, funded by FEDER/Junta de Andalucía-Consejería de Transformación Económica, Industria, Conocimiento y Universidades.
The authors thank Dräger Iberia (Madrid, Spain) and the local police of Granada City (Granada, Spain) for loan of the Dräger DrugTest 5000 and the Dräger Alcotest 6820 breath analyzer (Dräger Safety AG & Co. KGaA. Lübeck, Germany), and Pago de Almaraes wineries for providing us with the wine used in the study.

Two lines of space reserved to include
codes of the symposium and of this communication

The influence of visual function on driving performance under the influence of alcohol

Miriam Casares López*, José Juan Castro Torres, Sonia Ortiz Peregrina, Francesco Martino, Luis Jiménez del Barco

[1]*Department of Optics, Faculty of Sciences, University of Granada, Av. Fuente Nueva s/n, 18071, Granada, Spain.*

*e-mail: clmiriam@ugr.es

Purpose: Driving is a complex task that involves different motor and cognitive abilities. One of these is the visual function, responsible for 83% of the most important driving behaviours [1]. Driving under the influence (DUI) of alcohol is a frequent behaviour among drivers, however this substance deteriorates vision [2,3], which could negatively impact driving. Thus, the aim of this study was to assess the impact of a moderate-high alcohol dose on vision and driving performance, and to analyse the association between visual function and driving under the influence of alcohol.

Methods: a total of 34 participants (17 females), with ages ranging from 20 to 34 years, took part in the experiment. They took two experimental sessions: one in normal conditions (with no alcohol consumption), and a second one after the intake of 450 ml of red wine (approximately 48.6 g of alcohol). Thirty minutes after alcohol intake, the breath alcohol concentration (BrAC) was measured every 20 minutes (mean ± SD; 0.32 ± 0.12 mg/l) with a breath analyzer. In the two sessions, different visual functions were assessed: contrast sensitivity for 6 spatial frequencies (0.75, 1.5, 3, 6, 12, and 18 cpd), the visual discrimination capacity by means of the visual disturbance index (VDI) [4], and the optical quality by means of the MTF-cut off frequency for 4 mm pupil size using a double-pass system, the Optical Quality Analysis System (OQAS II). The driving performance was assessed with the Simax driving simulator v4.0.8 [5]. The scenario was a mountain road of single-lane single carriageway (6 km). The variables analyzed were the standard deviation of lateral position (SDLP, m), the standard deviation (SD) of the angular velocity of the steering wheel (rad/s), and the reaction time (s). An overall visual performance score (OVPS) and an overall driving performance score (ODPS) were calculated from the vision and driving results.

Results: The visual discrimination capacity was significantly impaired under the influence of alcohol on monocular and binocular viewing conditions ($p = 0.004$ and $p < 0.001$ respectively). The mean contrast sensitivity was also reduced in monocular and binocular viewing conditions ($p = 0.001$ and $p < 0.001$ respectively) for all special frequencies ($p \leq 0.001$). The MTF cut-off frequency was significantly reduced following alcohol consumption ($p < 0.001$). Regarding driving performance, an increase of the SDLP was observed, but the change was not significant ($p = 0.080$); the SD of the angular velocity of the steering wheel increased ($p = 0.001$), and the response time was also higher under the effects of alcohol ($p = 0.013$). The ODPS was significantly correlated with the OVPS ($\rho = 0.271$; $p = 0.026$).

Conclusions: Visual function, evaluated by means of the contrast sensitivity, the visual discrimination capacity, and the optical quality, was significantly impaired by the intake of a moderate-high dose of alcohol. Driving performance was impaired as well, and the driving ability was positively correlated with the visual performance under the influence of alcohol. These results highlight the fact that these features of visual function should be taking into consideration to ensure safe driving.

[1] McKnight AJ, Adams BB. *Driver education task analysis. Volume I: task description. Final report.* (1970).
[2] Casares-Lopez M, Castro-Torres JJ, Ortiz-Peregrina S, Martino F, Ortiz C. Changes in Visual Performance under the Effects of Moderate-High Alcohol Consumption: The Influence of Biological Sex. *International Journal of Environmental Research and Public Health* **18**(13), 15 (2021).
[3] Watten RG, Lie I. Visual functions and acute ingestion of alcohol. *Ophthalmic and Physiological Optics* **16**(6), 460 (1996).
[4] Castro JJ, Ortiz C, Pozo AM, Anera RG, Soler M. A visual test based on a freeware software for quantifying and displaying night-vision disturbances: study in subjects after alcohol consumption. *Theoretical Biology and Medical Modelling* **11** (2014).
[5] Ortiz C, Ortiz-Peregrina S, Castro JJ, Casares-Lopez M, Salas C. Driver distraction by smartphone use (WhatsApp) in different age groups. *Accident Analysis and Prevention* **117**, 239 (2018).

Acknowledgements: The authors thank Dräger Iberia (Madrid, Spain) and Local Police of Granada City (Granada, Spain) for lending us the Dräger Alcotest 6820 breath analyzer (Dräger Safety AG & Co. KGaA. Lübeck, Germany) and Pago de Almaraes wineries for providing us with the wine used in the study. This study was supported by Research Projects PID2020-115184RB-I00, funded by MCIN/AEI/10.13039/501100011033, and A-FQM-532-UGR2, funded by FEDER/Junta de Andalucía-Consejería de Transformación Económica, Industria, Conocimiento y Universidades.

Two lines of space reserved to include
codes of the symposium and of this communication

Periodic blur fluctuations effect on contrast sensitivity

Vahid Pourreza Ghoushchi*, Juan Mompeán, Pedro M. Prieto, Pablo Artal

Laboratorio de Óptica, Universidad de Murcia, Murcia, Spain.

*e-mail: vahid@um.es

This study investigates the resilience of human vision to the blurring effect induced by defocus oscillations. We applied sinusoidal oscillations in defocus with a range of amplitudes and temporal frequencies and determined the loss in contrast sensitivity. By inducing these defocus oscillations, we could compare them with natural accommodation fluctuations. We measured contrast sensitivity at 12 c/deg monocularly in five young, healthy emmetropic subjects through a tunable lens introducing sinusoidal oscillations of defocus around 0 D at 5, 15, and 25 Hz. Peak-to-peak oscillation amplitude varied from 0.15 D to 3 D. The visual stimulus was a Gabor patch at 3 m, and a two-choice forced-choice protocol was used. Target presentations were randomized through temporal frequency, amplitude, and contrast. The tunable lens was attached to an open-view Hartmann-Shack wavefront sensor [1,2] measuring in real time, thus allowing a) verification of the subject's accommodative state and b) confirmation of the amplitude and frequency of defocus oscillations generated by the lens.

The figure 1 illustrates the average contrast threshold as a function of amplitude for all subjects. Although there was some variability between subjects, contrast sensitivity was fairly constant despite the defocus oscillations introduced. Only for the fastest oscillations (25 Hz) and highest amplitude (+/-1.5 D) contrast sensitivity appears to suffer a relevant degradation.

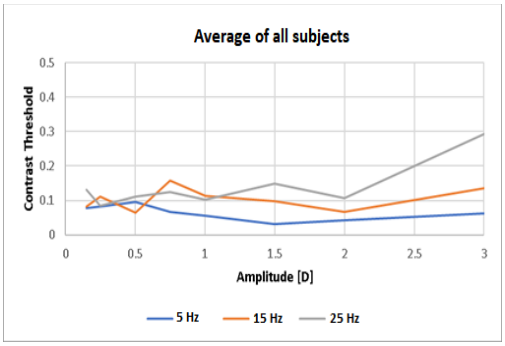

Figure 1. Mean contrast threshold for various defocus oscillations. The contrast sensitivity was fairly constant among the amplitudes introduced.

The data indicate that contrast sensitivity is resilient to induced periodic defocus. The fact that contrast sensitivity only appears to fall for fast and large oscillations in defocus suggests that the eye does not average blur and a short time with the image in or around the focus is enough to detect the target. These results have applications in electronic eyeglasses, visual simulators functioning based on fast periodic oscillations, and have implications in myopia control.

[1] V. P. Ghoushchi, J. Mompeán, P. M. Prieto, and P. Artal, Binocular dynamics of accommodation, convergence, and pupil size in myopes, *Biomed. Opt. Express* **12**, 3282 (2021).
[2] J. Mompeán, J. L. Aragón, P. M. Prieto, and P. Artal, GPU-based processing of Hartmann–Shack images for accurate and high-speed ocular wavefront sensing, *Futur. Gener. Comput. Syst.* **91**, 177 (2019).

Two lines of space reserved to include
codes of the symposium and of this communication

Personalized computational models with OCT. Challenges and opportunities

A. de Castro[1, *], E. Martinez-Enriquez[1], P. Urizar[1,2], S. Marcos[1,3]

[1]*Instituto de Óptica, Consejo Superior de Investigaciones Científicas, Calle Serrano 121, Madrid, Spain.*
[2]*2Eyesvision, Plaza de la Encina 10, Tres cantos, Madrid, Spain.*
[3]*Center for Visual Science. The Institute of Optics, University of Rochester, 361 Meliora Hall, NY, USA.*

*e-mail: a.decastro@csic.es

The optics of the human eye can be modelled on a personalized basis with precise knowledge of the geometry of the cornea and crystalline lens surfaces and their index of refraction. While there has been interest in the development of personalized eye models during decades with Purkinje [1,2], Scheimpflug [3,4] or Optical Coherence Tomography images (OCT) [5], these eye models are not being used in clinical settings due to several disadvantages, such as the optical corrections needed to quantify the surfaces of the eye or the uncertainties in the knowledge of the gradient refractive index of the crystalline lens.

With the improvement on image quality and acquisition speed, OCT has become ubiquitous in the eye clinic, where this technique is used to image the retina and the anterior segment of the eye. In our group we have developed algorithms to segment the anterior and posterior surfaces of the cornea and the crystalline lens and to correct the optical distortions present in the image. However, OCT is a point scanning technique and motion can occur during the time a full volumetric scan. We have recently developed a model to simulate the acquisition of data and to study the influence of eye movements that can be used to quantify the precision achieved with different scanning patterns and to design eye motion correction algorithms.

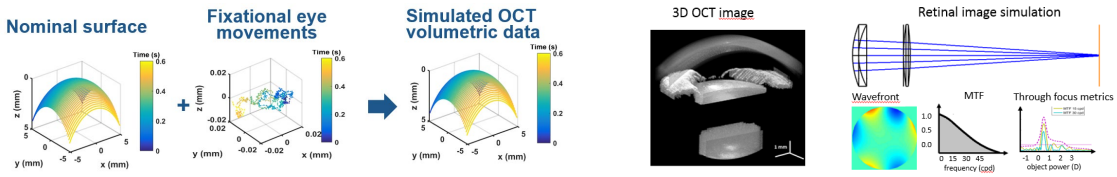

Figure 1. Left: OCT acquisition of the elevation is sequential and takes 0.6 seconds for one of our devices. Our model generates fixational eye movements in that time interval to simulate the OCT data acquired. Right: Volumetric image of the anterior segment and simulation of the retinal image with ray tracing software to study the optics of the post-cataract surgery optical system.

One of the applications of personalized eye models is to predict the outcome of a cataract surgery [6–8]. In this procedure, the crystalline lens is replaced by an intraocular lens (IOL) permanently and current methods to select the optical power of the IOL to implant rely on the outcome of previous surgeries and on assumptions regarding the corneal shape or the estimated lens position. IOL power formulas include empirical constants and need corrections in patients who do not meet the original assumptions of geometric relations in the eye (e.g. post-corneal surgery patients or very short or long axial lengths). In addition, when several IOL designs are possible, the decision of which IOL will be implanted is based on discussions about patient's need and expectations and not in the interactions between the lens design and the expected post-surgical corneal aberrations.

While in the clinical practice the process to select the IOL to be implanted have been improved over the years, computer eye models could be used for simulation of true retinal image quality with a particular IOL design on a personalized basis, allowing more accurate calculations of the optimal IOL power and a more customized IOL selection.

[1] J. Tabernero, P. Piers, A. Benito, M. Redondo, and P. Artal, *Invest Ophthalmol Vis Sci* **47**, 4651 (2006).
[2] P. Rosales and S. Marcos, *Opt Express* **15**, 2204 (2007).
[3] S. Norrby, *Ophthalmic and Physiological Optics* **25**, 153 (2005).
[4]. P. Rosales and S. Marcos, *J Refract Surg* **25**, 421 (2009).
[5] S. Ortiz, P. Perez-Merino, S. Duran, M. Velasco-Ocana, J. Birkenfeld, A. de Castro, I. Jimenez-Alfaro, and S. Marcos, Biomed *Opt Express* **4**, 387 (2013).
[6] C. Canovas and P. Artal, *Biomedical Optics Express* **2**, 1649 (2011).
[7] E. Martinez-Enriquez, P. Pérez-Merino, S. Durán-Poveda, I. Jiménez-Alfaro, and S. Marcos, *Scientific Reports* **8**, 9829 (2018).
[8] S. Marcos, E. Martinez-Enriquez, M. Vinas, A. de Castro, C. Dorronsoro, S. P. Bang, G. Yoon, and P. Artal, *Annual Review of Biomedical Engineering* **23**, 277 (2021).

Acknowledgements: PID2020-115191RB-100, IND2019/BMD-17262, H2020-ICT-2017 779960, NIH NIE P30EY 001319.

Enhanced second harmonic imaging of the living human eye using deconvolution

Rosa M. Martínez-Ojeda[1,*], Laurent M. Mugnier[2], Pablo Artal[1], Juan M. Bueno[1]

[1]*Laboratorio de Óptica, Universidad de Murcia, 30100 Murcia, Spain.*
[2]*ONERA / DOTA, Université Paris Saclay, F-92322 Châtillon, France.*

*e-mail: rosamaria.martinez9@um.es

Second harmonic generation (SHG) imaging is a form of nonlinear (or multiphoton) microscopy providing intrinsic confocality and reduced photodamage, without the use of staining procedures [1]. It is useful to visualize collagen-based tissues, in particular those of the eye [2]. Although broadly used with *ex vivo* samples, its implementation to image living human ocular structures has been successfully reported [3]. However, the presence of aberrations, scattering and non-controlled eye movements limit the imaging performance of this technique. Here, we present a deconvolution procedure to deal with these limitations and improve the quality of *in vivo* SHG images.

The 2nd generation of a compact clinically-adapted SHG microscope was developed to acquire images (0.45s exposure time) from different locations of the cornea and sclera of the living human eye. The whole system was controlled through custom software. The average laser power of the pulse illumination beam was 20 mW, more than 10 times below the maximum permissible exposure (according to ANSI Z136.1-2000). An image processing approach based on a marginal blind deconvolution algorithm [4] was applied to improve contrast and resolution of the recorded SHG images. It is based on a sound statistical framework that avoids the usual degeneracies encountered in blind deconvolution and makes it entirely unsupervised. Original and deconvolved images were compared and evaluated with different quality metrics.

The procedure was able to enhance the quality of the images independently of their location. As an example, Figure 1 compares SHG images before and after deconvolution. This leads to a better visualization of biological details while keeping the total intensity constant (i.e., energy conservation). Although the effectiveness and the increase in quality depended on the metric used, the improvement was readily observable for all imaged areas of the eye.

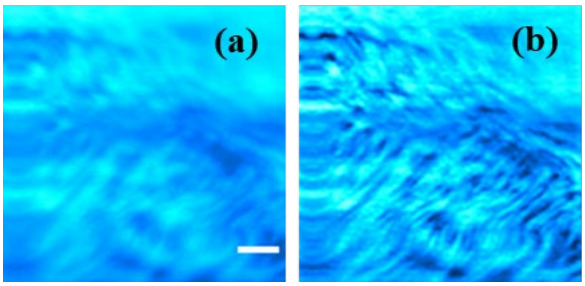

Figure 1. SHG images of the living human eye before (a) and after (b) deconvolution. Bar length: 50 μm.

In conclusion, a blind deconvolution scheme to enhance SHG images of the *in vivo* human eye has been presented. Details on the sample's morphology and structure that couldn't be observed in the original images were visible in the restored ones. Since collagen fibers are better visualized and their spatial distributions accurately assessed, this technique might serve as a clinical tool for early detection of pathologies associated with microscopic changes in tissue organization.

[1] Fine and Hansen, *Appl. Opt.* **10**, 2350 (1971).
[2] Bueno, Gualda and Artal, *Cornea* **30**, 692 (2011).
[3] Ávila, Gambín, Artal and Bueno, *Sci. Rep.* **9**, 10121 (2019).
[4] Blanco and Mugnier, *Opt. Express*, **19**, 23227 (2011).

Acknowledgements: This work was supported by the Agencia Estatal de Investigación, Spain (grants PID2019-105684RB-I00 and PID2020-113919RB-I00).

Two lines of space reserved to include
codes of the symposium and of this communication

Optical sectioning in microscopy with structured illumination and single pixel detection

Luis Ordóñez*, Erick Ipus, Armin J. M. Lenz, Jesús Lancis, Enrique Tajahuerce

GROC-UJI, Institute of New Imaging Technologies (INIT), Universitat Jaume I, 12071, Castelló, Spain
*e-mail: lordonez@uji.es

The impact of microscopy has undergone an enormous advance in science. This could not be possible without new technologies that can increase the image resolution, allow us to measure many optical parameters such as the fluorescence emission, optical phase, wavelength, or polarization state, permit high-speed capture rates, and improve the penetration capability in scattering media [1]. In this work we design a new microscope with optical sectioning properties by combining two structured illumination techniques: structured illumination microscopy (SIM) and single-pixel imaging (SPI). As a first application we introduce optical sectioning capability on single-pixel fluorescence microscopy.

SIM techniques increase the image resolution and provides sectioning capability in conventional microscopy methods [2]. By projecting a small number of high frequency periodic fringe patterns with different phase onto the sample and combining the obtained images with the proper phase-shifting algorithm, it is possible to exclude the out of focus areas from the final image.

SPI techniques scan the scene with a set of structured light patterns while the transmitted, reflected, or fluorescence light is detected with a bucket detector [3]. They are advantageous for multidimensional imaging as well as in situations where the amount of light is scarce or a high temporal resolution is required [3]. In our optical configuration we use a DMD to project the light patterns onto the sample, which codify Walsh-Hadamard functions, and a photomultiplier tube (PMT) to detect the fluorescence light emitted by the sample.

Combining SIM and SPI makes optical sectioning possible in imaging with a bucket detector. The key idea is to employ a grating located before the photodetector. This configuration is designed starting from the conventional SIM configuration and exploiting the principle of Helmholtz reciprocity.

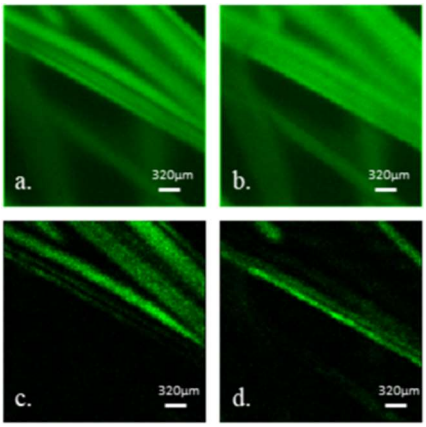

Figure 1. **(a)** and **(b)** are images of cotton fibres obtained with conventional single-pixel microscopy for two different focusing planes located at $z = 0$ and $10\mu m$, respectively. **(c)** and **(d)** are images of the same sample planes obtained with our microscope with optical sectioning.

Preliminary results of the fluorescent SPI and SIM techniques are presented (Fig. 1.) The sample is a set of cotton fibres with green fluorescent ink. Figures 1(a) and (b) show images of the sample focused on different depths, with an axial separation of 10 µm, obtained with a conventional single-pixel microscopy. The two images show cotton fibres located at different distances that appear strongly defocused. Figures 1(c) and (d) show images of the same planes of the sample but obtained with the new single-pixel microscopy technique. Now only the focused cotton fibres in each axial plane are clearly visible. All images have a size of 128x128 pixels.

In summary, we present the principles and implementation of a SPI fluorescence microscope with optical sectioning based on a SIM technique. By combining the high-speed binary modulation of the DMD, a high frequency grating, and the high photosensitivity of the PMT, we are able to image fluorescence samples using structured illumination. Our experimental results show an optical sectioning capability similar to that obtained with conventional SIM techniques with a digital camera.

[1] J. Mertz; *Introduction to Optical Microscopy* (Cambridge University Press, 2019).
[2] D. Dan et al., "DMD-based-LED-illumination super-resolution and optical sectioning microscopy," Sci. Rep. **3**, 1116 (2013).
[3] M.P. Edgar et al., "Principles and prospects for single-pixel imaging," Nat. Photon. **13**, 13-20 (2019).

Acknowledgements: We acknowledge financial support from Agencia Estatal de Investigación (PID2019-110927RB-I00/AEI/10.13039/501100011033) and Generalitat Valenciana (PROMETEO/2020/029, ACIF/2019/019).

Advances in Fourier Lightfield Microscopy

Manuel Martínez-Corral

3D Imaging and Display Lab., Department of Optics, University of Valencia, 46100 Burjassot, Spain.

e-mail: Manuel.martinez@uv.es

Conventional microscopes have the ability of capturing 2D images of small specimen with high magnification and spatial resolution. This feature is determined by the numerical aperture (NA) of the microscope objective. The main drawback of conventional microscopes is their poor performance for imaging 3D structures. This lack is somehow overcame by capturing stacks of depth images and computing from them the 3D image. The main disadvantage of this procedure is the need of an axial scanning.

In the past few years Lightfield Microscopy (LFM) is showing to be a powerful tool for the recovery of 3D images of samples in a high-speed regime. In few words, an LFM is the result of inserting a microlens array (MLA) at the image plane of a conventional microscope. The images captured by the LFM are composed by a collection of microimages, one per microlens, which store the spatial and de angular information of the light emitted by the sample. Then, a collection of perspective images is computed from the microimages. The main drawback of LFMs is that they provide, after the hybrid (optical plus computational) procedure, images with a spatial resolution that is about 10 times worse that than of the host microscope. Other drawback is the inhomogeneous lateral resolution of computed depth sections. Naturally, much work has been reported aiming to overcome these drawbacks by computational means.

To overcome these drawbacks, Fourier Lightfield Microscopy (FLMic) was proposed. In FLMic the perspective images are captured directly, have a spatial resolution that is about 3 times better than that of LFMs, and have shift invariance. This allows the direct use of deconvolution tools and to avoid the inhomogeneity of depth sections. Other advantage of FLMic is that it can be implemented by inserting an ad-on at one microscope port, and therefore allows to makes use of all the facilities of the microscope.

Along the past few years FLMic has attracted a great interest in the scientific and technological community due to its potential utility in the observation of 3D dynamic processes.

In this contribution we explain the ray-optics theory behind Lightfield concept, and combine it with the wave-optics nature of microscopy applications. We show, also, how to compute these images for obtaining refocused depth images, and also 3D depth maps. Finally, the most recent contributions are reviewed.

[1] B. Javidi et al., Roadmap on 3D integral imaging: Sensing, processing, and display, *Optics Express* **28**, 32266 (2020).

[2] M. Martinez-Corral and B. Javidi, Fundamentals of 3D imaging and displays: a tutorial on integral imaging, light-field, and plenoptic systems, *Advances in Optics and Photonics* **10**, 512 (2018).

Acknowledgements: This research was funded by Grant RTI2018-099041-B-I00, which is cofounded by the Ministerio de Ciencia, Innovacion y Universidades (Spain) and by European Regional Development Fund; by Generalitat Valenciana (Spain) under Grant PROMETEO/2019/048.

Two lines of space reserved to include
codes of the symposium and of this communication

Quantum imaging with a photon number resolving camera

Víctor Bernardo Puente

Hamamatsu Photonics France, Spain & Portugal office, C. Argenters 4 edif 2,
Parque Tecnológico del Vallés, 08290 Cerdanyola, Spain.

e-mail: vbernardo@hamamatsu.es

We wish to demonstrate the application of a qCMOS detector, capable of performing quantum enhanced imaging by photon counting. Presenting this work will be beneficial in allowing investigators consider the potential applications of the qCMOS technology in the quantum imaging domain.

Until now, quantum enhanced imaging schemes were realized through correlations between single photons. Due to the limiting readout noise of CCD and CMOS technologies, our ability to count photons was reduced to distinguishing between zero photons and one or more. Acquisition speeds were therefore limited by both the readout rate of the detector array, and the necessity of operating in an extremely sparse regime.

However, the recent development of a qCMOS camera that is capable of photon number resolving due to its low readout noise, has enabled quantum enhanced imaging at higher illumination regimes. Operating in such a way will allow an increased data acquisition rate, accelerating the development of quantum enhanced imaging schemes for their implementation into end-user technologies.

Two lines of space reserved to include
codes of the symposium and of this communication

Computer generated training datasets for deep learning applications to ESPI fringe patterns, using true speckle simulation

J. M. Crespo *, V. Moreno

QMatterPhotonics Research Group. Optics Area. Department of Applied Physics. Faculty of Physics / Faculty of Optics and Optometry. University of Santiago de Compostela. E-15782 Santiago de Compostela. Galicia. Spain.

*e-mail: josemanuel.crespo.continas@rai.usc.es

Over the last few years, the ongoing innovation in the field of artificial intelligence (AI) and artificial neural networks (ANN), as well as the development of IT frameworks such as Tensorflow, PyTorch and Keras, have eased the application of these techniques in different fields of scientific research. This simplification in the tools and the reduction of costs of specialized hardware platforms, allows the application of this technology by researchers and students, reducing the workload to develop those AI systems to focus on the problem to solve, and not on the tools supporting that resolution.

Specifically in the field of optical interferometry, these systems have great possibilities for noise removal and image cleaning [1,2], although their great drawback is the need for large datasets of images for training. While for application in biomedical sciences or satellite image processing there are open databases to use in the training phases. In the field of interferometry these training sets are scarce and limited, making necessary generate the training sets using simulation techniques.

Our interferometric use case to apply these AI techniques is the electronic speckle pattern interferometry (ESPI), widely used as optical metrology technique to measure displacement and deformation measurement. Noise, and low visibility are major drawbacks for this technique and the AI has been proved as disruptive technique to enhance and mitigate those major drawbacks.

The ESPI fringe pattern is obtained from a pair of images, I and I', taken from a specimen under study before and after deformation. The fringe pattern is obtained subtracting those images and the resulting intensity pattern is according to the formula [3]

$$|I - I'| = 4\sqrt{I_o I_r}\,\sin\left(\phi_o - \phi_r + \frac{\varphi}{2}\right)\sin\left(\frac{\varphi}{2}\right)$$

with I_o, I_r, ϕ_o, and ϕ_r the amplitude and phase of the object and reference speckle fields, and φ is the optical phase difference induced by the deformation. For the estimation of φ our approach is to use random Zernike polynomials to build the random phase, $\varphi = \sum_0^n c_i Z_i$, where c_i and Z_i are a random coefficient and the i-Zernike polynomial respectively and n is the order of the Zernike expansion. With this approach, any displacement field can be simulated, setting the proper interval for c_i and moreover, selecting the order of the Zernike expansion will control the complexity of the simulated displacement.

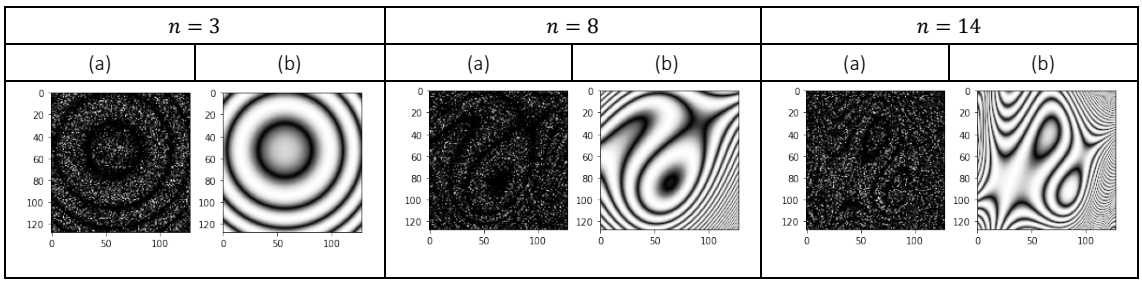

Figure 1. Generated images using Zernike order (n=3, 8, 14) showing increasing complexity. (a) ESPI image using equation (1) and speckle simulation according to the method described by J Goodman [3]. (b) Clean $\sin(\varphi/2)$.

[1] Fungui Hao, Chen Tang, Ming Xu, *Applied Optics* **58**, 3338 (2019).
[2] Crespo J. M., Moreno V., Rabuñal Juan Ramón, Pazos Alejandro, Canabal Carbia Monica. *EOS Annual Meeting (EOSAM 2020)*,115 (2020)
[3] Joseph W. Goodman, *Speckle phenomena in optics*, SPIE (2020).

Two lines of space reserved to include
codes of the symposium and of this communication

Desarrollo de un sistema de procesado láser 3D asistido por robot para la eliminación de pintura.

Angel Rodríguez, Ana J. López*, Javier Lamas, Alicia Moreno, Alberto Ramil

Laboratorio de Aplicacións Industriais do Láser, Campus Industrial de Ferrol, Universidade da Coruña. 15471, Ferrol, A Coruña, España.

*e-mail: ana.xesus.lopez@udc.es

La limpieza con láser es una técnica que permite la eliminación controlada de contaminantes superficiales de un material. Desde la década de los 80, se ha aplicado en diferentes campos industriales, como el aeroespacial, automoción, así como en biomedicina, o la conservación del Patrimonio Cultural, entre otros[1,2]. En comparación con los métodos convencionales, la limpieza láser tiene la ventaja de ser una técnica selectiva sin contacto y respetuosa con el medio ambiente. Además, combinada con robots industriales, puede utilizarse para eliminar con precisión los contaminantes en estructuras grandes y complejas, lo que mejora en gran medida la calidad y la eficiencia de la técnica. Sin embargo, el procesado láser automatizado de superficies no planas o superficies 3D no es un tema completamente resuelto y la mayoría de las soluciones propuestas se basan en aproximaciones cuasi 3D o 2.5D[3]. En este trabajo se presenta un sistema de limpieza láser asistido por robot para el procesado de superficies 3D, basado en la integración de un brazo robótico de 6 grados de libertad (6 DOF) con un láser de pulsos ultracortos y un sistema de captura tridimensional de la superficie que permite generar automáticamente las trayectorias del haz láser sobre la superficie asegurando en todo momento la incidencia normal y el control de los distintos parámetros del proceso[4]. El manipulador de 6 GDL permite tanto el desplazamiento como el cambio de orientación del objeto para que el procesado láser se lleve a cabo siguiendo las rutas programadas en una verdadera solución 3D[5]. Tanto el software como el hardware para coordinar el robot y el encendido/apagado del láser fueron desarrollados con enfoque FOSS y, en la medida de lo posible OSHW. Los resultados experimentales muestran la efectividad del sistema propuesto que mejora la eficiencia de la limpieza láser automatizada de objetos 3D y permite su aplicación a otros procesos de ablación láser como el micromecanizado o estructurado de superficies.

[1] Rivas T, Pozo S, Fiorucci MP, López AJ, Ramil A. Nd:YVO4 laser removal of graffiti from granite. Influence of paint and rock properties on cleaning efficacy. *Applied Surface Science* **263**, 563 (2012). https://doi.org/10.1016/j.apsusc.2012.09.110.
[2] Zhang D, Xu J, Li Z, Li K, Wang C, Shan D, et al. Removal mechanism of blue paint on aluminum alloy substrate during surface cleaning using nanosecond pulsed laser. *Optics and Laser Technology* **149** (2022). https://doi.org/10.1016/J.OPTLASTEC.2022.107882.
[3] López AJ, Lamas J, Pozo-Antonio JS, Rivas T, Ramil A. Development of processing strategies for 3D controlled laser ablation: Application to the cleaning of stonework surfaces. *Optics and Lasers in Engineering* **126**, 105897 (2020). https://doi.org/10.1016/J.OPTLASENG.2019.105897.
[4] Lamas J, Ramil A, Yañez A. Smoothing and simplification algorithm for Computer Aided Manufacturing paths with complex curves. *IFAC Proceedings Volumes* (IFAC-PapersOnline), vol. 4, IFAC Secretariat, p. 61 (2009). https://doi.org/10.3182/20091006-3-es-4010.00013.
[5] Rodríguez A, López AJ, Lamas J, Moreno A, Ramil A. Development of a laser cleaning robot system for the processing of 3D surfaces. In: Negahdaripour S, Stella E, Ceglarek D, Möller C, editors. *Multimodal Sensing and Artificial Intelligence: Technologies and Applications II*, SPIE, p. 28 (2021). https://doi.org/10.1117/12.2592111.

Agradecimientos: Este trabajo ha sido parcialmente financiado por el Ministerio de Economía y Competitividad a través del Proyecto BIA2017 8589 R

Two lines of space reserved to include
codes of the symposium and of this communication

Manipulating the second order coherence function for super-resolution intensity correlation imaging

Enrique J. Fernandez*, Iryna Standret, Pien Vinke, Juan M. Bueno

Laboratorio de Óptica, Instituto Universitario de Investigación en Óptica y Nanofísica, Universidad de Murcia, Campus de Espinardo (Edificio 34), E-30100, Murcia, Spain

*e-mail: enriquej@um.es

The Hanbury Brown-Twiss (HB-T) effect evidenced the existence of correlations in the near instantaneous intensities measured at separated space and time points of the light emitted from a thermal light source [1]. The quantum interpretation of the effect was capital for the development and understanding of photon entanglement. Intensity correlation imaging, in both classical and quantum frame, uses second-order or higher coherence of entangled photons, for instance in ghost imaging. In general, two-photon and intensity correlation imaging modalities can be modelled as the convolution of the aperture function of the object with the second order coherence function $G^{(2)}$ [2]:

$$R_{im}(\vec{r}_{im}) = \int_{OBJ} d\vec{r}_{obj} \left| Aper(\vec{r}_{obj}) \right|^2 G^{(2)}(\vec{r}_{obj}, \vec{r}_{im}).$$

In this work we demonstrated a system with a modified second order coherence function $G^{(2)}$ to increase the spatial resolution in intensity correlation imaging modalities. Figure 1 shows a diagram of the experimental set up. By using a paraxial biprism, two virtual images S_1 and S_2 from a thermal light source S_0 were created. A CCD camera was placed in the zone of light intersection from virtual sources after the prism. The second order coherence function $G^{(2)}$ was obtained from sets of images by performing light correlations across pixels in the sensor with short exposure time, preventing the average of the incoming light. The experimental function $G^{(2)}$ obtained with and without the biprism are shown in Figure 2 in the right and left panel, respectively. The comparison of the FWHMs of the functions yielded a near 5.5 factor difference. In addition, this factor could be controlled by changing the effective distance from the source S_0 to the prism. The significant thinning of the $G^{(2)}$ function can boost resolution for intensity correlation imaging modalities, further surpassing the classical limit of diffraction.

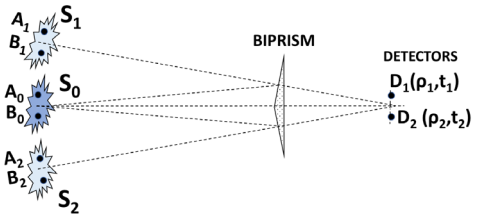

Figure 1. S_0 represents a chaotic light source generated by the rotating diffuser. S_1 and S_2 are the virtual images generated by the paraxial biprism from object S_0. After the biprism the pixels of the CCD camera acted as independent detectors.

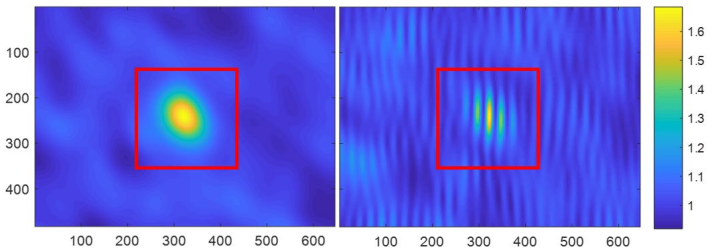

Figure 2. Left: experimental function $G^{(2)}$ obtained from S_0 (i.e. no biprism). Right: $G^{(2)}$ obtained when the biprism generated the virtual images S_1 and S_2. In both cases, axes correspond to pixels on the camera sensor (2 µm/pix).

[1] R. Hanbury Brown and R. Q. Twiss, *Nature* **177**, 27 (1956).
[2] Y. Shih, *An Introduction to Quantum Optics, Photon and Biphoton Physics*, 2nd Edition, CRC Press, (2021).

Acknowledgements: This work was supported by Ministerio de Ciencia e Innovación, Agencia Estatal de Investigación, Spain (PID2020-113919RB-I00).

Two lines of space reserved to include
codes of the symposium and of this communication

Visual acuity in phakic and monofocal pseudophakic eyes under red, green, and blue lights

Laura Clavé[1,2,*], Aurora Torrents[2], Miquel Ralló[2], María S. Millán[2]

[1]*Hospital de Mataró, Servicio de Oftalmología, Consorci Sanitari del Maresme, 08304 Mataró, España.*
[2]*Grupo de Óptica Aplicada y Procesado de Imagen, Departamento de Óptica y Optometría, Universitat Politècnica de Catalunya-BARCELONATECH, Terrassa, España.*

*e-mail: lclave@csdm.cat

Introduction: Chromatic aberration of the human eye is caused by the dependence of the refractive index of the ocular media on the wavelength. The replacement of the natural lens of the eye by an intraocular lens might modify the longitudinal chromatic aberration (LCA) of the pseudophakic eye, depending on the chromatic dispersion of the lens material as well as other design features of the implant.[1] Most studies report LCA data as chromatic difference of refraction, but the impact of LCA on the visual acuity (VA) has been scarcely studied, particularly in pseudophakic patients.[2]

Purpose: To assess and compare the impact of quasi-monochromatic illumination on the VA of young phakic and monofocal pseudophakic subjects using red (R), green (G), and blue (B) wavelengths.

Methods: 31 young phakics aged 23.06± 5,11years, with accommodation preserved, and 30 pseudophakics aged 68.64 ± 9.52 years, implanted with a monofocal intraocular lens (Y601075, AJL Ophthalmic, Spain), participated in this study. Distance VA was measured with custom optotype illuminated sequentially with B (455nm), G (530nm), R (625nm), and white (W) LED lights. [2] Near VA was additionally assessed in young phakic eyes under the same illuminations. All VA measurements were taken monocularly and are reported in logMAR scale. Statistical analysis was performed and P-values under 0.05 were considered statistically significant.

Results:

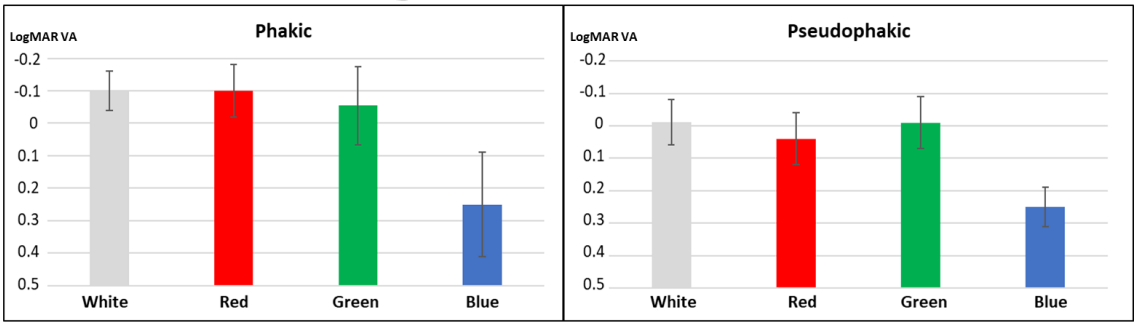

Figure 1: Distance VA under W, R, G, and B lights (mean, SD): (left) phakic group, (right) pseudophakic group.

Discussion: Clinical VA assessment under separated R, G, and B lights allowed the detection of tiny but significant variations in the chromatic difference of refraction existing in phakic and monofocal pseudophakic patients. Pseudophakic patients reached their maximum distance VA under G (used in intraocular power calculation to target postoperative refraction) and W lights. Young phakic subjects, however, reached their maximum distance VA under R illumination (equal to the one obtained with white light) thanks to the combination of LCA and some accommodative effort. Yet for them, the mean near VAs showed balanced results under R, G, and B illuminations, [2] thus adapting their accommodative effort to the chromatic difference of power.

[1] M. Vinas-Pena, A. de Castro, C. Dorronsoro et al., Understanding in vivo chromatic aberrations in pseudophakic eyes using on bench and computational approaches, *Photonics* **9**, 226 (2022).
[2] L. Clavé, A. Torrents, M. Ralló, M.S. Millán, Visual acuity assessment in phakic and pseudophakic eyes under red, green, and blue illumination, *Opt. Pura Apl.* **53**(4), (2020).

Acknowledgements: Agencia Estatal de Investigación (PID2020-114582RB-I00/ AEI / 10.13039/501100011033)

Two lines of space reserved to include
codes of the symposium and of this communication

Jacobi Fourier Polynomials: more flexibility for designing ophthalmic solutions

Eva Acosta[1], Enrique Gonzalez-Amador[1, 2], Justo Arines[1,*]

[1]*Department of Applied Physics, University of Santiago de Compostela, Faculty of Optics and Optometry.*
[2]*Universidad Politécnica de Tulancingo, Ingenierías No. 100, 43629, Tulancingo, Hidalgo, México.*

e-mail: justo.arines@usc.es

Researchers working in Visual and Ophthalmic Optics are used to work with orthogonal basis to develop optical solutions to improve instrumentation for imaging different structures of the eye or to design lenses to improve people's visual quality. Zernike polynomials (ZP) are the most outstanding basis in this field. Although presenting several advantages in some applications due to their relationship with optical aberrations, the radial dependence of ZP consist in a polynomial of a given integer degree. In this work we add a degree of freedom to the radial dependence by using a subset of Jacobi Polynomials (JP) while keeping the same angular dependence of ZP. We will show the improvement for the correction of refractive errors by numerical simulation of retinal images. We define the Jacobi Fourier Polynomials by [1]:

$$JF(n,p,q,r,\theta) = J_n(p,q,r)\begin{Bmatrix}\cos(m\theta)\\ \sin(m\theta)\end{Bmatrix} = \sqrt{\frac{w(p,q,r)}{b_n(p,q)}}G_n(p,q,r)\begin{Bmatrix}\cos(m\theta)\\ \sin(m\theta)\end{Bmatrix}$$

where, r and θ are the radial and angular coordinates respectively, $J_n(p,q,r)$ are the Jacobi polynomials, $w(p,q,r)$ is the weighting function, and $b_n(p,q)$ the normalization factor. The parameters p and q must obey $(p-q) > -1$ and $q > 0$. Details on the expression of $w(p,q,r)$, $b_n(p,q)$ and $G_n(p,q,r)$ can be found in [1]. As an example, for the particular case with $p = q = 7$, $n = 0$ and $m = 3$, we get that $JFP(r,\theta) = \sqrt{7}r^3\cos(3\theta)$ is proportional to Zernike $Z_3^3(r,\theta)$ also known as trefoil aberration and commonly used to increase the depth of focus of optical systems [2]. In this work we will keep the azimuthal frequency m=3 and change the radial dependence through p, q and n.

We present our study on the use of a phase in the shape of a JFP added to that of an intra ocular lens, or a contact lens to obtain optical solutions to presbyopia. To study its effect on retinal images, we performed numerical simulations in MATLAB2022a. We used computational Fourier Optics to simulate the images generated by a presbyopic eye and optotypes placed at different vergences within the interval [0,5] D for three different pupil diameters (7,5,3) mm and two different magnitudes of primary spherical aberration (SA) with peak to valley (P-V) values of 0.15 µm and -0.15 µm within a pupil of 5 mm diameter. We compared the performance of the naked eye and that with different JFP with $n = 0$ and $p = q = [7, 8, 9, 10]$ with P-V values of 30 µm and 60 µm at 5 mm pupil diameter. We will also show values for different objective visual criteria: VSOTF, Visual Strehl combined, and image correlation.

Our results show that the extension of the range of clear vision is better with JFP phase with the advantage that it does not depend on the pupil diameter. The centre of the range of clear vision depends on the value of the SA, but it could be adjusted by adding some amount of defocus. Figure 1 shows an example of the images obtained for the naked eye (left) for a JFP phase (right).

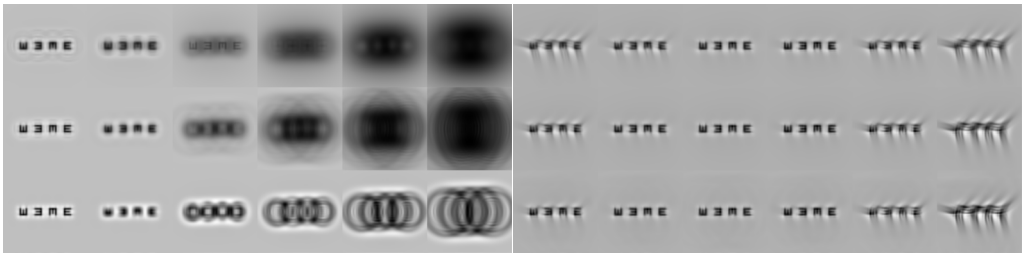

Figure 1. Left: Retinal images for naked eye. Right: Retinal Images obtained with *n=0* and *p=q=8*, P-V = 30µm. In both cases object vergences from 0D to 5D; pupil diameters D= (7,5,3) mm and +0.15 SA.

[1] E. González-Amador, et al., *Optics and Lasers in Engineering* **126**, 105880 (2020).
[2] J. Arines, et al., *Optics Letters* **39**, 3986 (2014).

Two lines of space reserved to include
codes of the symposium and of this communication

Optical coherence tomography in retinitis pigmentosa patients treated with an injection of autologous bone-marrow-derived mononuclear stem cells

A. Vanesa García-Navarro[1,2], M. Elena Rodríguez[2], Juan M. Bueno[1,*]

[1]*Laboratorio de Óptica, Universidad de Murcia, 30100 Murcia, Spain.*
[2]*Servicio de Oftalmología, Hospital Universitario Virgen de la Arrixaca, 30120 Murcia, Spain.*

*e-mail: bueno@um.es

Retinitis pigmentosa (RP) is a genetic retinal pathology affecting the outer retina [1]. It involves a progressive death of photoreceptors, with loss of central visual acuity and reduction of pigment epithelial functions. Although there's no cure for RP, treatments such as gene therapy and retinal implants are being tested. In particular, a novel treatment based on an intravitreal injection of human bone-marrow-derived mononuclear stem cells (BM-MSCs) is for retinal dystrophy that has been demonstrated promising in both humans and animal models [2,3]. In this study we analyzed the physiological changes at the central macula produced in a set of patients suffering from advanced RP, treated with a single intravitreal injection of autologous BM-MSCs.

The clinical trial was carried out at the Hospital Universitario "Virgen de la Arrixaca" in Murcia (Spain). Eight patients (mean age: 37±11) suffering from advanced RP were involved in the study. Each volunteer received an intravitreal injection of autologous BM-MSCs in one of their eyes. An injection of saline solution (placebo) was injected in the contralateral eye. Patients underwent a complete ophthalmologic test including optical coherence tomography (OCT) imaging (CIRRUS, Carl ZEISS). Evaluation was performed one day before the injection (basal visit) and at different time points during the 12-month follow-up period.

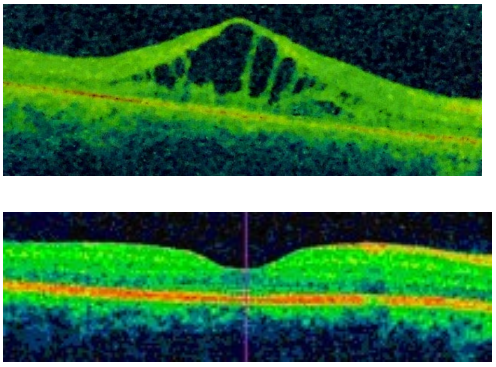

Figure 1. OCT images of a patient suffering from advanced RP (top) and a control subject (bottom). The edema related to the pathological stage is clearly visualized.

At the basal visit (i.e., before injection) measurements in both eyes often showed larger foveal thickness values (>300 μm on average) than those corresponding to normal subjects, what is typically associated to the macular edema present in some RP subjects (see Figure 1). After the injection, the temporal evolution of the retinal thickness was assessed. It is interesting to notice that in patients with thicker edemas there was a reduction in foveal thickness between the basal and the last visit. However, since the initial thickness was different for each patient, the evolution after the treatment with autologous BM-MSCs varies among them. Results show that after 1 year of treatment, most of patients fairly benefit from the therapy, since the central foveal thickness is often reduced or maintained.

In conclusion, this study shows that although the cure of RP has still a challenge, the treatment with a single injection of autologous BM-MSC is reliable, feasible and safe, with possibilities of success. This treatment may have a potential therapeutic effect since it might be useful to reduce the effects of the macular edema and to decrease central macular thickness. Under this perspective, stem cell therapy is an alternative to be developed and merits further investigation.

[1] R. A. Pagon, *Surv. Ophthalmol.* **33**, 137 (1988).
[2] J. B. Jonas, M. Witzens-Harig, L. Arsenievand A. D. Ho, *Acta Ophthalmol.* **86**, 225 (2008).
[3] J. Di Pierdomenico, D. García-Ayuso, M. E. Rodríguez, et al. *Int. J. Mol. Sci.* **21**, 7252 (2020).

Acknowledgements: This work was supported by Ministerio de Ciencia e Innovación, Agencia Estatal de Investigación, Spain (PID2020-113919RB-I00).

Two lines of space reserved to include
codes of the symposium and of this communication

Caracterización cromática de una lente intraocular comercial de foco extendido

Diego Montagud-Martínez[1,*], Vicente Ferrando[1], Anabel Martínez-Espert[2, 3], Juan A. Monsoriu[1], Walter D. Furlan[2]

[1]*Centro de Tecnologías Físicas, Universitat Politècnica de València, 46022 Valencia, Spain;* [2]*Departamento de Óptica y Optometría y Ciencias de la Visión, Universitat de València, 46100 Valencia, Spain;* [3]*Clínica Aiken, Fundación Aiken, 46004 Valencia, Spain.*

*e-mail: diemonma@upvnet.upv.es

Gracias a las nuevas tecnologías, como ordenadores, tablets o smartphones, las demandas visuales de los pacientes en distancias intermedias se han incrementado. Debido a esto las lentes intraoculares (IOLs) de foco extendido (EDOF) están en auge ya que presentan un buen rendimiento visual en distancias lejanas e intermedias. Muchas de estas IOLs utilizan óptica difractiva en su diseño [1, 2]. Para caracterizar las propiedades ópticas de estas lentes es importante hacer un estudio policromático con diferentes longitudes de onda.

El objetivo de este trabajo es comprender cual es la estrategia de diseño empleada por la lente comercial EDOF AT LARA 829MP para conseguir la extensión de foco.

Para ello se midieron las propiedades ópticas de la lente para tres longitudes de onda 450 nm, 550 nm, 650 nm y con luz policromática en un banco óptico que cumple la norma ISO 11979-2, 2014 [3] para una pupila de 4.5 mm. Se calcularon las TF-MTFs para 50 líneas por mm y las PSFs y se obtuvieron las imágenes de un test USAF en diferentes vergencias.

Como se puede observar en la Figura 1, la IOL muestra un comportamiento cromático claramente diferente en función de la longitud de onda. Mientras que para el verde presenta un perfil bifocal con ambos focos de altura similar, para el rojo y el azul los perfiles se asemejan más al de una lente monofocal y estos se sitúan entre los dos focos verdes. Por otro lado, la línea negra (luz policromática) muestra el perfil EDOF de la IOL.

La lente EDOF AT LARA 829MP está diseñada para diferentes longitudes de onda, presentando un perfil bifocal para la luz verde, mientras que muestra un perfil monofocal para el rojo y azul. Por tanto, este diseño utiliza las diferentes longitudes de onda para generar un perfil policromático de foco extendido de aproximadamente 2.0 D.

[1] Zvorničanin, J.; Zvorničanin, E.; Premium intraocular lenses: The past, present and future. *J. Curr. Ophthalmol.* **30**, 287 (2018).
[2] Rampat, R.; Gatinel, D. Multifocal and extended depth-of-focus intraocular lenses in 2020. *Ophthalmology* **128**, e164 (2020).
[3] ISO 11979-2. Ophthalmic Implants-Intraocular Lenses-Part 2: Optical Properties and Test Methods. International Organization for Standardization: London, UK, 2014.

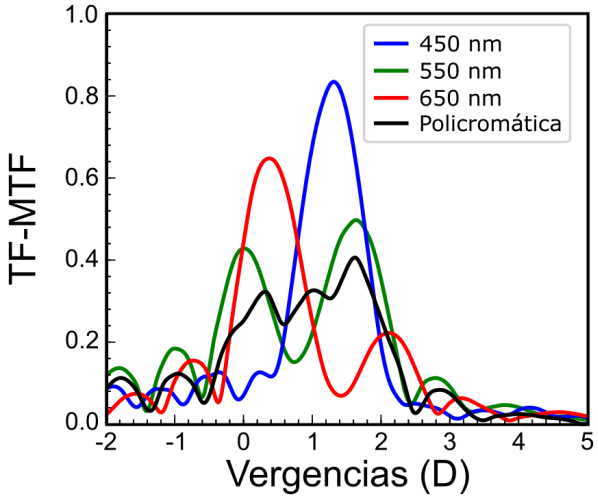

Figura 1. TF-MTF para las tres longitudes de onda y con luz policromática de la IOL AT LARA 829MP en pupila de 4.5 mm

Agradecimientos: Diego Montagud-Martínez agradece la financiación otorgada por la beca Margarita Salas del Ministerio de Universidades de España financiado por the European Union-Next Generation EU

Two lines of space reserved to include
codes of the symposium and of this communication

Impacto de la aberración esférica en modelos de ojos teóricos

Anabel Martínez-Espert[1,2,*], Diego Montagud-Martínez[1,3], Vicente Ferrando[3], Juan A. Monsoriu[3], Walter D. Furlan[1]

[1]*Departmento de Óptica y Optometría y Ciencias de la Visión, Universitat de València, 46100 Valencia, España.* [2]*Clínica Aiken, Fundación Aiken, 46004 Valencia, España.* [3]*Centro de Tecnologías Físicas, Universitat Politécnica de València, 46022 Valencia, España.*

*e-mail: amares9@alumni.uv.es

Los modelos de ojo son sistemas utilizados para comprender el funcionamiento de las superficies del ojo [1]. En el área de la óptica fisiológica el uso de modelos de ojos teóricos tiene múltiples aplicaciones, entre ellas, la evaluación teórica de diferentes elementos ópticos, como lentes intraoculares (LIOs). Para realizarla se utilizan programas de trazado de rayos que permiten evaluar la calidad óptica del elemento de estudio. Existen numerosos modelos de ojos teóricos publicados en la literatura científica [1-3]. En ellos, a medida que aumenta la complejidad del sistema los resultados obtenidos se aproximan más a las condiciones clínicas reales. Uno de los modelos más utilizados es el de Liou-Brennan (LB) [2], cuyos parámetros se basan en datos biométricos de pacientes con una media de 45 años. Uno de los parámetros que varía entre los diferentes modelos es la asfericidad (Q), la cual genera aberración esférica (AE) [3]. La norma ISO 11979:2014 [4] especifica los requisitos y métodos de ensayo para determinar las propiedades ópticas de las LIOs. A la hora de evaluarlas de forma teórica LIOs, es posible utilizar los parámetros de dicha norma como un modelo de ojo teórico.

El objetivo del presente estudio es comparar numéricamente el efecto de la AE en tres modelos: El de LB, y dos configuraciones de la norma ISO 11979:2014 [4]. La primera configuración (ISO 1) no presenta AE total (AE= 0.00 µm), mientras que la segunda configuración (ISO 2) tiene una AE total similar a la de LB (AE = 0.28 µm).

Para estudiarlo, se ha utilizado el software de trazado de rayos Zemax (OpticStudio; versión 18.7, LLC, Kirkland, WA, EEUU). Se han programado dos lentes monofocales con diferente Q en la cara posterior y potencia de 20 D. La primera monofocal se programó con una Q = -3.65 que compensa la AE de la configuración ISO 1. Mientras que la segunda monofocal compensa la AE del modelo de LB (Q = -7.85). Se calcularon la *Modulation Transfer Function* (MTF) en el plano focal del modelo, para frecuencias espaciales entre 0 y 60 ciclos/mm (Figura 1). También se realizó una evaluación de los *Spot diagrams* para observar los resultados en el plano focal. La configuración ISO 2 y el modelo de LB presentan un comportamiento similar ya que la Q global de ambos modelos es similar. Sin embargo, hay diferencias entre ambas configuraciones debido a que el ojo teórico de LB es un modelo más complejo que no presenta simetría de revolución. Se observa que al neutralizar la AE en los tres modelos, el comportamiento es similar en los tres casos. Por tanto, la AE es una de las mayores diferencias entre modelos de ojos teóricos.

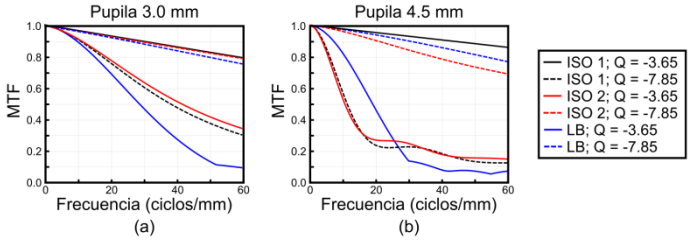

Figura 1. MTFs en el plano focal de los diferentes ojos modelo con (a) 3 mm y (b) 4,5 mm de pupila.

[1] Polans, J.; Jaeken, B.; McNabb, R.P.; Artal, P.; Izatt, J. A. *Optica* **2**, 124 (2015).
[2] Liou, H.L.; Brennan, N.A. *J Opt Soc Am A* **14**, 1684 (1997).
[3] Atchison, D.A. Handbook of Visual Optics, Taylor & Francis Group (2017).
[4] ISO 11979-2:2014. Ophthalmic implants-Intraocular lenses-Part 2: Optical proprieties and test methods.

Agradecimientos: Diego Montagud-Martínez agrade a la beca Margarita Salas del Ministerio de Universidades de España financiado por the European Union-Next Generation EU.

Two lines of space reserved to include
codes of the symposium and of this communication

Analysis of the accommodation response as a supporting tool during subjective refraction

Aina Turull-Mallofré*, Carlos E. García-Guerra, Mikel Aldaba, Meritxell Vilaseca, Jaume Pujol

Center for Sensors, Instruments and Systems Development, Universitat Politècnica de Catalunya.
Rambla Sant Nebridi 10, 08222 Terrassa, Spain.

*e-mail: aina.turull@upc.edu

The refraction process aims to find the combination of sphero-cylindrical lenses that maximizes visual acuity with minimum accommodation. The gold standard technique for assessing refraction is subjective refraction, which includes the control of accommodation by means of fogging technique. Despite the importance of accommodation in the refraction process, there is little knowledge on how the accommodative status behaves during the subjective refraction. For this reason, the main purpose of this work was to analyse the accommodation response during subjective refraction in order to obtain the accommodative status when the patient was wearing the subjective refraction. Moreover, we also aimed to find the relationship of the transition point between relaxed and activated accommodation and the subjective refraction, to determine if the information obtained could be used as a supporting tool for the subjective refraction technique.

Thirty healthy young adults between 18 and 30 years old participated in the study. The accommodation response of the right eye was monitored during a sweep of spherical lenses while wearing the subjective refraction. The set-up to monitor the accommodation consisted of a Hartmann-Shack aberrometer coupled to a phoropter that worked as an open-filed instrument and had a monitoring frequency of 10 Hz [1].

A sweep of lenses from +1.50 D to -1.50 D, in steps of 0.25 D relative to the patient's subjective refraction, was presented in front of the corrected eye while monitoring accommodation. The relative accommodation was calculated as the difference between the value of accommodation measured for each induced power of the sweep of lenses (ΔS) and the minimum measured accommodation. For the subjective refraction, the relative accommodation was obtained for ΔS=0. In figure 1, an example of the accommodation as a function of the sweep lenses is shown, where the solid line represents the measured accommodative response. With the aim to obtain the point of transition between the relaxed and activated accommodation two linear fitting were obtained for each ΔS, the first considering the curve between -1.50 D and ΔS, and the second between ΔS and +1.50 D. In figure 1, the curve fitting for ΔS=0 is shown, corresponding to the dashed lines. The induced power ΔS that produced the best cumulative coefficient of determination was chosen as the transition point between relaxed and activated accommodation, as in Figure 1, indicated with the red point.

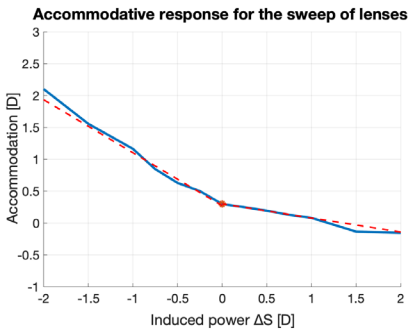

Figure 1. Accommodative response during the sweep of lenses.

The mean relative accommodation ± SD obtained when wearing the subjective refraction was 0.38 ± 0.20 D. The agreement between the value of the traditional subjective and the value of refraction that was in the phoropter in the transition of accommodation obtained by means of the linear fitting was analysed with the Bland-Altmann test. The mean ± SD of the difference between methods and 95% limits of agreement were 0.041 ± 0.41 D (0.84 D, -0.76 D).

We can conclude that there is a tendency of having a residual activated accommodation with the subjective refraction. Moreover, the point of transition between relaxed and activated accommodation may be a significant information to be used during subjective refraction to enhance the procedure and to detect accommodation-related problems during the visual examination.

[1] C. E. García-Guerra, J. Martínez-Roda, M. Aldaba, S. Galera, C. Aransay, F. Díaz-Doutón, J. Pujol, M. Vilaseca; Real-time monitoring of accommodation during subjective refraction, *Invest. Ophthalmol. Vis. Sci.* **61**(7), 1716. (2020).

Acknowledgements: This publication is part of the project PID2020-112527RB-I00, funded by MCIN/AEI/10.13039/501100011033.

Two lines of space reserved to include
codes of the symposium and of this communication

Visual simulation and correction using economic and compact vertical aligned liquid crystal devices

Alba M. Paniagua-Diaz[1,*], Juan Mompean[1], Juan L. Aragon[2], Pablo Artal[1]

[1]Laboratorio de Óptica, Centro de Investigación en Óptica y Nanofísica (CiOyN), Universidad de Murcia, Campus de Espinardo (Ed. 34), 30010 Murcia, Spain. [2]Departamento de Ingeniería y Tecnología de Computadores, Universidad de Murcia, Campus de Espinardo, Murcia 30100, Spain.

*e-mail: a.paniagua-diaz@um.es

In this work we demonstrate the potential of Vertical-Aligned Spatial Light Modulators (SLM) in the simulation and correction of High Order Aberrations (HOA) by testing visual acuity and the contrast sensitivity function in a set of healthy subjects. We perform Visual Acuity (VA) and Contrast Sensitivity function (CS) tests in different subjects, with their vision corrected by the AO system and with the phase map of severe keratoconus (RMS >1 for 5 mm diameter pupil). The applicability of this modulation device for visual adaptive optics correction and simulation is discussed.

Spatial Light Modulators (SLMs) have been responsible for important advances in different applications of Adaptive Optics (AO) such as vision, since they became widely available [1,2]. These devices can essentially modify the amplitude and/or phase of an incident wavefront, although phase-only modulation is the most widely used feature due to its efficiency and versatility. Most widely used SLMs are composed of a Liquid Crystal (LC) device between two linear polarizers. Liquid crystal molecules can be vertically aligned (VA), parallel aligned (PA) or twisted (T), although for simplicity of use and quality, for phase-only applications PA-LCoS are the gold standard. VA-LCoS are typically used as high-contrast amplitude modulators [3], not holding a large depth of phase modulation, barely surpassing π radians. In a recent study it was shown how the use of two VA-LCoS arranged in series (thus allowing phase summation) could develop phase modulation outcomes very similar to those of the gold standard PA-LCoS, with a significant lower cost and improved compactness [4].

Methods: Figure 1 shows the setup used for testing the VA and CS with the phase-only modulation unit consisting of two VA-LCoS devices arranged in series. The optical components of this unit include: the two VA-LCoS modulators (SLM1 and SLM2) with their optical axis at 45º from the horizontal in operating conditions; a linear polarizer P oriented at 45º from the horizontal to achieve phase-only modulation. The plane of SLM1 is optically conjugated with SLM2 to easily implement the phase summation. The optical stimulus is placed at 2.8 meters from the aperture of the system. The aperture has a diameter of 5mm and is conjugated to the surface of the SLMs. The modulated pupil is finally conjugated with the eye's pupil plane. A beam splitter (BS) in front of the eye opens an extra path for a pupil camera, monitoring the centering of the eye in the system.

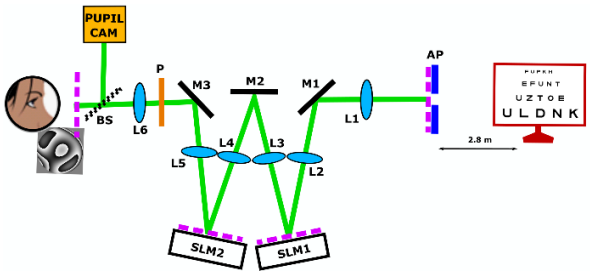

Figure 1. Optical setup for the phase-modulation testing with two VA-LCoS devices arranged in series, whilst evaluating the visual acuity and contrast sensitivity function of different subjects. The conjugated planes are depicted by the pink dashed line.

Results: The results from the VA and CS tests showed a clear difference between the values of VA and CS with the simulated keratoconus, being on average 0.6 points better the corrected VA vs the keratoconus simulated one. In the case of the CS, we found a consistent average drop of 0.35 points in the corrected vs the keratoconus simulated one, in agreement with the expected vision degradation with high-order RMS increase [6].

Conclusions: In this work we demonstrate the capabilities of the VA-LCoS modulation unit for the simulation of HOA and the correction of vision in an open-view configuration. These results pave the way for the use of economic and compact VA-LCoS devices in the correction of vision based on adaptive optics, both for low and high order aberrations.

[1] S. Marcos *et al*., *Vision Research* **132**, 3 (2017).
[2] C. Schwarz *et al.*, *Optics Letters* **36**(24), 4779 (2011).
[3] D. Cuypers *et al.*, *IEEE/OSA Journal of Display Technology* **7**(3), 127(2011).
[4] A. Arias *et al.*, *Optics Express* **28**, 34180 (2020).
[5] A. B. Watson & A. J. Ahumada, *Journal of Vision* **8**(4), 17 (2008).

Two lines of space reserved to include
codes of the symposium and of this communication

Straylight and Optical Memory Effect characterization of ex-vivo cataractous crystalline lenses

Dulce Simón[1], Alba M. Paniagua-Díaz[1,*], Carmen Martínez[1], Elena Moreno[1], Alba Rodríguez-Ródenas[1], Inés Yago[2], José María Marín[2], Pablo Artal[1]

[1]*Laboratorio de Óptica, Universidad de Murcia, Campus de Espinardo, 30100 Murcia, Spain.*
[2]*Oftalmología, Hospital Universitario "Virgen de La Arrixaca", El Palmar, Murcia, Spain.*

*e-mail: a.paniagua-diaz@um.es

Cataracts increase the amount of intraocular light scattering in the crystalline lens causing vision impairment by blurring and reducing the contrast in the retinal images. Wavefront shaping techniques in combination with the Optical Memory Effect have been suggested for the optical (non-surgical) correction of scattering in cataractous lenses [1]. In this context, we aim to characterize the scattering properties of excised human lenses by measuring their OME.

Methods: The Optical Memory Effect (OME) is an intrinsic correlation of scattering media that provides the isoplanatic patch of a cataract's correction imaging technique, determining how the transmitted speckle pattern changes with a tilt/shift of the incident beam [2]. We measured this using a 594-nm laser incident on different cataractous lenses by recording the transmitted speckle pattern for different values of tilt/shift and comparing them via cross-correlation. For each cataract stage, we also characterized scattering using the straylight parameter, measured with the Optical Integration Method [3], and the Michelson Contrast of the images obtained. A total of 34 lenses of donors aged between 29 and 67 were measured.

Results: There is a linear relationship between the straylight parameter, image contrast and OME decorrelation (Fig.1d-f), providing a new tool for the prediction of the OME range when only quantitative scattering measurements are taken. In severe cataracts (straylight parameter Log10[s]>2), the OME provides an isoplanatic patch of about 1 degree in tilt and 400 µm in shift, a range that is linearly increased as the optical cataract decreases.

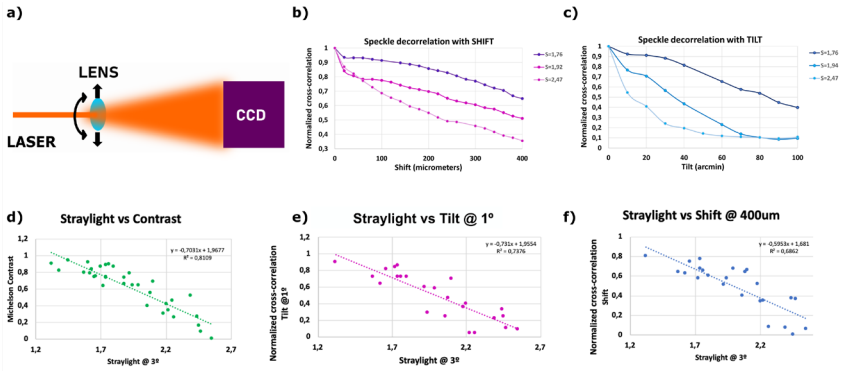

Figure 1. a) Schematic of the experimental configuration for the measurement of the shift and tilt OME. b) Normalized cross-correlation of the transmitted speckle patterns for different values of lateral translation (or shift), in steps of 20 µm. The different curves represent three different crystalline lenses with straylight parameters at 3 degrees of 1,76, 1,92 and 2,47, from quasi transparent to opaque. c) Normalized cross-correlation of the transmitted speckle patterns for different values of tilt, in steps of 10 arcmin, for the different lenses. d-f) Graphs showing the relationship between the Straylight at 3 degrees with the Michelson contrast (d), normalized cross-correlation for a tilt of 1 degree (e) and the normalized cross-correlation for a shift of 400 um (f).

Conclusions: The OME of cataractous excised human lenses has been measured for the first time and is found to be non-negligible for cataracts, being strongly dependent on the scattering strength. This work paves the way to approaches for the non-invasive and real-time correction of cataracts with wearable devices.

[1] Paniagua-Díaz, A. M. *et al*., *Optics Express* **29**(25), 42208 (2021).
[2] Osnabrugge, G. *et al*., *Optica* **4**(8), 886 (2017).
[3] Ginis, H. *et al*., *J. Vis.* **12**(3), 20 (2012).

Two lines of space reserved to include
codes of the symposium and of this communication

Effects of small residual astigmatism on the reading performance of contact lens neophytes

Pedro Gil[1,2,*], Alexandra Farcas[2], Celia Hernández[2], Antonio Benito[2], Juan Tabernero[1,2]

[1]*Departmento de Electromagnetismo y Electrónica, Universidad de Murcia, 30100 Murcia, Spain.*
[2]*Laboratorio de Óptica, Universidad de Murcia, 30100 Murcia, Spain.*

*e-mail: pedro.gilf@um.es

The purpose of this work is to compare the effect of toric contact lenses (full corrections of astigmatism) versus spherical soft contact lenses (corrected with the mean spherical equivalent refraction) on the reading performance of novel contact lens (CL) users with low astigmatism.

The reading test consisted of two paragraphs of 92 and 97 words divided into six lines (Arial 10 font) shown on a 23.6" screen at a reading distance of 60 cm and corresponding to a visual acuity (VA) of 0.65. Reading performance parameters (reading time, number and duration of fixations, number of regressions and magnitude of saccades) were recorded using an eye tracking device (GP3 HD, Gazepoint, Vancouver, Canada) at a frequency of 150 Hz. Additionally, contrast sensitivity (CS) at 9 and 15 cpd, respectively, and VA, VA at 40 cm and VA at 60 cm were measured with a Visual Adaptative Optics simulator (VAO; Voptica SL, Murcia, Spain).

Forty contact lens neophytes were recruited. They were divided into two groups, matched by age and refractive error (no statistically significant differences). Subjects in group one (N=21; age 21 ± 4 years; sphere -2.3 ± 0.8 D; cylinder -1.0 ± 0.3 D) were monocularly fitted with a spherical contact lens (Precision1, Alcon Laboratories, Inc, Fort Worth, TX) while subjects in group two (N=19; age 21 ± 4 years; sphere -2.5 ± 1.4 D; cylinder -0.9 ± 0.3 D) were fitted with a toric lens (Precision1 for Astigmatism).

Subjects in the toric group showed a significant improvement ($p < 0.05$) in VA and CS at 9 cpd ($p < 0.05$). Some reading performance magnitudes like the proportion of regressions (Fig. 1) and the mean duration of fixations showed a similar tendency, being slightly worse in the group fitted with spherical lenses, but no significant differences were found.

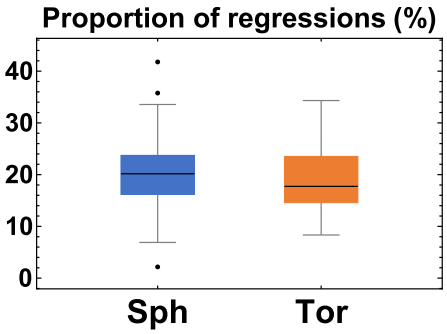

Figure 1. Between-group comparison of the proportion of regressions in reading.

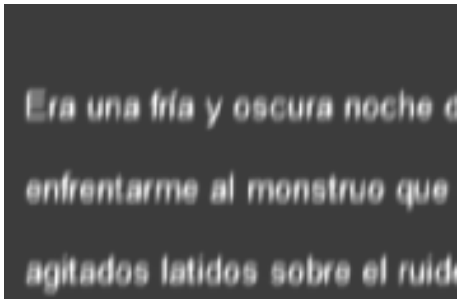

Figure 2. Optical simulation of the reading test for the average subject in the spherical CL group (pupil diameter = 4.5 mm).

In conclusion, subjects with the toric fit showed better VA and CS and tended to perform slightly better in the reading test, but variability was large between subjects. This may be because the text under the conditions previously described is still legible (see optical simulations in Fig. 2) for spherical lens users with low to moderate astigmatism. Rotations and decentrations of the toric lens may explain why the visual perception of the text may look similar between subjects in both groups.

Acknowledgements: Grant PID2019-105639RA-I00 (Ministerio de Ciencia, Innovación y Universidades, Spain) and a predoctoral grant (21602/FPI/21) from Fundación Séneca, Región de Murcia, Spain.

Numerical analysis of cross-talk phenomena in pixelated PA-LCos devices

Adriana R. Sánchez-Montes[1,*], Jorge Francés[1,2], Andrés Márquez[1,2]

[1]*Instituto Universitario de Física Aplicada a las Ciencias y las Tecnologías, Universidad de Alicante, Spain.*

[2]*Departamento de Física, Ingeniería de Sistemas y Teoría de la Señal, Universidad de Alicante, Spain.*

*e-mail: adrianaros.sanchez@gcloud.ua.es

The new technological developments and their impact on both the increase of the resolution and the reduction of the pixel sizes on parallel-aligned liquid crystal on silicon (PA-LCoS) microdisplays have made PA-LCoS a promising candidate for phase-only modulation and spatial light modulators (SLMs) applications. The pixel grid pattern on PA-LCoS induces several phenomena, i.e. the electric field crosstalk in the interpixel region, also known as fringing fields, out-of-plane reorientation of the liquid crystal director, and diffraction effects due to interpixel region. Here, a rigorous numerical methodology has been applied to avoid simplified models that neglect these kinds of phenomena. More specifically, the Frank-Oseen elastic free energy has been minimised to find the optimal LC director distribution [1]. This analysis has been carried on in a three-dimensional domain, taking into account the external field's influence on the pixel. Once the LC director distribution has been estimated, the electrical permittivity tensor is derived and used for a complete three-dimensional Finite-difference time-domain method (FDTD) [2] analysis. The Stokes parameter is determined in reflection from the electromagnetic field computed by FDTD as a function of time and space.

Fig. 1 shows the Stokes parameters as a function of the external voltage for the pixel sizes of 5 and 7 μm. The fill factor (FF) is defined as the ratio of the active area of the pixel (i.e., without the interpixel gap area) and the entire area of the pixel in percentage. The interpixel gap sizes considered are 0.2, 0.4 and 0.6 μm dealing with fill-factor of 92%, 85% and 77% for the 5 μm pixel size, and 94%, 89%, and 84% for the 7 μm pixel size. Fig. 1(a)-(b) shows the S_1 parameter for 5 μm and 7 μm pixel sizes, respectively. A reduction of the deviation with respect to the infinite pixel (FF 100%) is considered for the largest pixel size. A similar trend can be perceived for the degree of polarization (DOP). The influence of pixel and interpixel sizes is not clear for S_2 and S_3 parameters. The numerical results here shown are consistent with the experimentation detailed in [3].

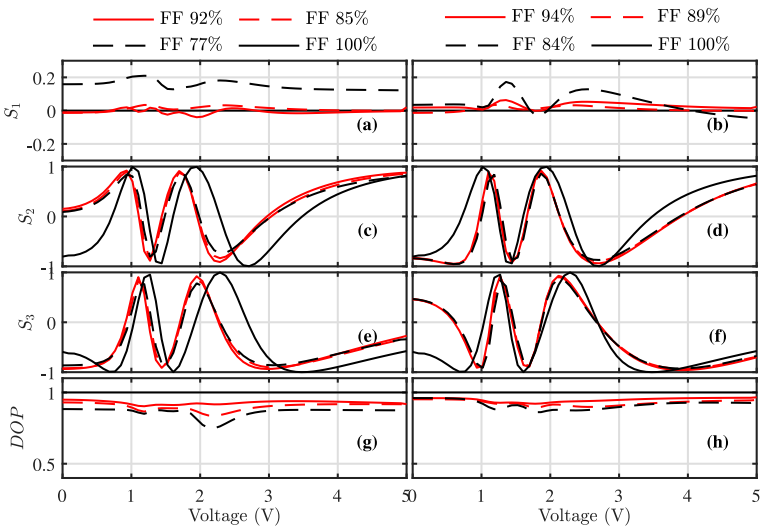

Figure 1. Stokes parameters as a function of external voltage for 5 μm pixel size (a),(c),(e) and (g), and 7 μm pixel size (b),(d),(f) and (h). Three different interpixel gaps are analysed 0.2, 0.4, and 0.6 μm.

References

[1] S. Moser *et al.*, *Opt. Express*, 27(**18**), 25046 (2019).

[2] J. Francés *et al.*, *Materials*, 13(**17**), (2020).

[3] A. Márquez *et al.*, *Opt. Lett.* 45(**20**), 5732-5735 (2020).

Acknowledgements: This work has been supported by Generalitat Valenciana (projects PROMETEO/2021/006; IDIFEDER/2021/014, cofunded by European Union through the FEDER programme). The corresponding author is grateful to the "Generalitat Valenciana" for the grant (GRISOLIAP/2021/106).

Precise-Integration Time-Domain for Optical Anisotropic Media

Joan Josep Sirvent-Verdú[1], Jorge Francés[1,2,*], Sergi Gallego[1,2], Augusto Beléndez[1,2]

[1] *Instituto Universitario de Física Aplicada a las Ciencias y las Tecnologías, Universidad de Alicante, España.*

[2] *Departamento de Física, Ingeniería de Sistemas y Teoría de la Señal, Universidad de Alicante, España.*

*e-mail: jfmonllor@ua.es

The Precise-Integration Time-Domain (PITD) formulation permits to break through the Courant-Friedrich-Levy (CFL) condition, which limits the accuracy, stability, and indirectly the applicability of the traditional Finite-Difference Time-Domain (FDTD) method. This characteristic permits considering larger time steps than the largest one fixed by the CFL condition. As the conventional FDTD scheme, PI also takes the spatial derivatives through the central finite-difference scheme. This step sets up a set of ordinary differential equations (ODEs) that are solved using the PI Technique [1,2,3]. However, as demonstrated in [4,5], considering larger time steps does not entirely fulfil the hypothesis of the expected reduction of running time simulations. Increasing the time step makes larger some coefficients of the sparse matrix **M**. The memory requirements for storing this matrix dramatically influence the method's performance. Even that, accurate results have been achieved with larger time steps up to six times larger than the upper boundary value fixed by the CFL condition. The results covered in [4,5] focused on validating the method in slits, thin-film filters, binary phase gratings, and twisted-nematic liquid crystal cells (TNLCs) demonstrated the method's accuracy. Here, the technique is applied to different periodic and anisotropic optical media. More precisely, to anisotropic polarization gratings (PG). PG is based on a periodically patterned, uniaxial birefringence in the grating plane that modulates the polarization of light instead of its amplitude [6].

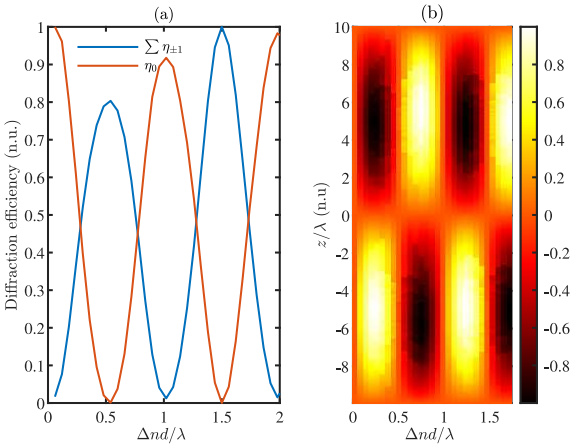

Figure 1. (a) Diffraction efficiency as a function of the normalized retardance. Setup fully defined in [5]. (b) S_4 parameter in the output plane as a function of the normalized retardance.

Fig. 1(a) shows the diffraction efficiency of the 0th- and ±1st-orders as a function of the normalized retardation $\Delta nd/\lambda$, where Δn is the birefringence, d the thickness of the PG, and λ the wavelength. The scheme simulated is fully defined in Fig. 7 in [6]. The results provided by Fig. 1(a) are close to those shown in Fig. 8(a) in [6]. Fig. 1(b) shows the behaviour of the PG when it is illuminated with a plane wave linearly-polarized. More precisely, Fig. 1(b) represents the Stokes parameter S_4 as a function of the normalized output plane (z/λ) and the normalized retardation $(\Delta nd/\lambda)$. The results are consistent with those shown in Fig. 9(a) in [6]. Right- and a PG produces left-handed circularly-polarized waves as a function of the normalized retardance parameter.

[1] Wan-Xie, Z., *J. Comput. Appl. Math*, **163**, 59 (2004).
[2] Zhong, W. X and Williams, F. W., *Proc. Inst. Mech. Eng. Part C J. Mech. Eng. Sci*, **208**, 427, (1994).
[3] X. Zhu, X. Ma, J. Shao, *IEEE Microw. Wirel. Compon. Lett.* **1309** (2021)
[4] Sirvent-Verdú, J.J *et al.*, *Materials* **14** (2021).
[5] Sirvent-Verdú, J.J., *Análisis numérico mediante la técnica de integración precisa en diferencias finitas: aplicación a dispositivos ópticos difractivos*, TFG (Universidad de Alicante), (2021).
[6] Oh, C. and Scuti, M., *Opt. Express*, 14(**24**), 11870 (2006).

Acknowledgements: The work was supported by Generalitat Valenciana (projects PROMETEO/2021/006; IDIFEDER/2021/014, cofunded by European Union through the FEDER programme).

Two lines of space reserved to include
codes of the symposium and of this communication

Investigating ergodicity for the determination of optical coherence functions

Iryna Standret*, Rosa M. Martínez-Ojeda, Juan M. Bueno, Enrique J. Fernandez

Laboratorio de Óptica, Instituto Universitario de Investigación en Óptica y Nanofísica, Universidad de Murcia, Campus de Espinardo (Edificio 34), E-30100, Murcia, Spain.

*e-mail: iryna.standret@um.es

Emission and detection of light are stochastic processes. Ergodicity is one of the most important concepts associated to these stochastic processes. In a stationary process one can assume to be under ergodic condition when the time average of a typical realization $u = {}^{k}x(t)$ of the stochastic process of any deterministic function $F(u)$ is identical to the corresponding ensemble average. Mathematically:

$$\left\langle F\left[{}^{k}x(t)\right]\right\rangle_{t} = \left\langle F\left[x(t)\right]\right\rangle_{E}.$$

In this work, we have experimentally determined under which conditions the temporal average is equivalent to a pseudo-ensemble average, populated of realizations of the stochastic process, for the calculation of the second degree of coherence $\gamma^{(2)}$. This function is of capital importance for certain imaging modalities, as ghost imaging. Its mathematical form is:

$$\gamma^{(2)}(r_1, r_2, t_1, t_2) = \frac{\langle I_1(r_1, t_1) \cdot I_2(r_2, t_2)\rangle}{\langle I_1(r_1, t_1)\rangle \cdot \langle I_2(r_2, t_2)\rangle}.$$

Figure 1 depicts the experimental system to measure the function $\gamma^{(2)}$. For the recording of the elements of the ensemble average, sequences of 100 frames each (exposure = 50 μs) were obtained. For the time average version of $\gamma^{(2)}$, sequences of increasing number of frames were retrieved. The function $\gamma^{(2)}$ can be characterized by its FWHM and height over the baseline. Figure 2 summarizes the results, showing both parameters obtained from pseudo-ensemble average and time average (blue and red, respectively).

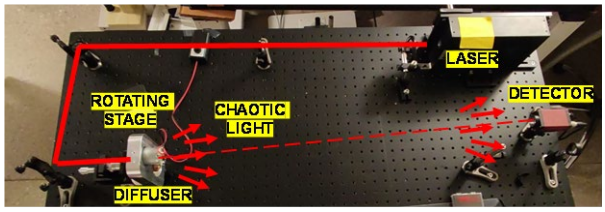

Figure 1. Experimental system compounded by a laser illuminating a rotating diffuser, which created a chaotic light source. A camera was placed in front of the so-generated pseudo-thermal light source.

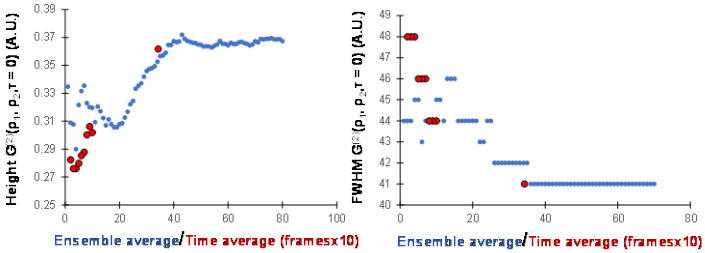

Figure 2. Height and FWHM of $\gamma^{(2)}$. Blue colour stands for ensemble average while red dots indicate time average.

We found that time averages above of 3500 frames reached steady values for the parameters of the $\gamma^{(2)}$. The methods and results are important to optimize the required number of frames in coherence functions, with application in ghost imaging.

[1] E. Wolf, *Introduction to the theory of coherence and polarization of light,* Cambridge University Press (2007).

Acknowledgements: This work was supported by Ministerio de Ciencia e Innovación, Agencia Estatal de Investigación, Spain (PID2020-113919RB-I00).

Two lines of space reserved to include
codes of the symposium and of this communication

Impact of the detector response on the temporal second degree of coherence of a chaotic light source

Pien Vinke*, Juan M. Bueno, Enrique J. Fernandez

Laboratorio de Óptica, Instituto Universitario de Investigación en Óptica y Nanofísica, Universidad de Murcia, Campus de Espinardo (Edificio 34), E-30100, Murcia, Spain.

*e-mail: p.vinke@um.es

The Hanbury and Brown-Twiss (HB-T) effect is a form of a non-trivial correlation in both time and space from a thermal or chaotic light source. It was first described in 1954 in the context of radioastronomy, to be soon after demonstrated in the visible range. A new type of interferometer was devised to characterize this effect [1]. This intensity interferometer correlates light signals measured from 2 detectors D_1 and D_2 at time t_1 and t_2, placed at positions ρ_1 and ρ_2. The resulting correlation function obtained in the HB-T interferometer is a version of the second degree of coherence function $\gamma^{(2)}$. The function $\gamma^{(2)}(\rho_1,t_1,\rho_2,t_2)$ allows to characterize the coherence and bunching of incoming photons. Modified versions of HB-T interferometers are used for non-conventional imaging, such as ghost imaging and quantum imaging. Intensity correlations in this context are referred to instantaneous measurements of light intensity, or photon annihilation. In the laboratory, real detectors always exhibit certain integration time t_c, which must be considered to correctly interpret the results of such intensity interferometers, or their counterpart light correlation imaging system [2]. In this work, we studied and experimentally characterized the impact of the detector response t_c on the retrieved temporal $\gamma^{(2)}$. To do so, a fiberized intensity interferometer with 2 avalanche photodiodes, classical version of the HB-T interferometer, was set and calibrated in the laboratory. A pseudothermal (chaotic) light source was generated by rotating a diffuser (48.6 rad/s) with grit index 1500, back illuminated by a 660 nm CW laser. Figure 1 presents two experimental $\gamma^{(2)}(\tau)$ obtained under t_c = 4 µs and t_c = 100 µs, with $\tau = t_1 - t_2$.

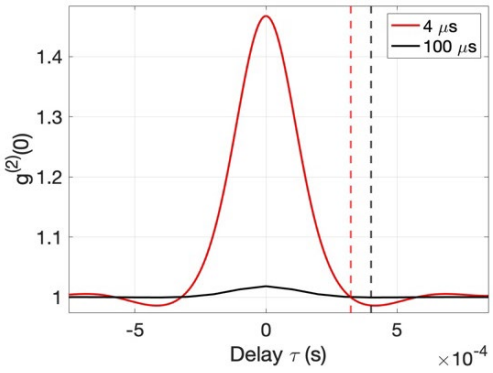

Figure 1. Second order temporal coherence function with t_c = 4 µs (red) and t_c = 100 µs (black). Dashed lines refer to τ_c.

Figure 2 presents $g^{(2)}(0)$ as a function of the ratio t_c/τ_c, with τ_c being the coherence time of the source. It was experimentally determined as:

$$f\left(\frac{t_c}{\tau_c}\right) = 3.03 \cdot 10^{-3} \cdot \frac{t_c}{\tau_c}^{-0.99} + 0.99$$

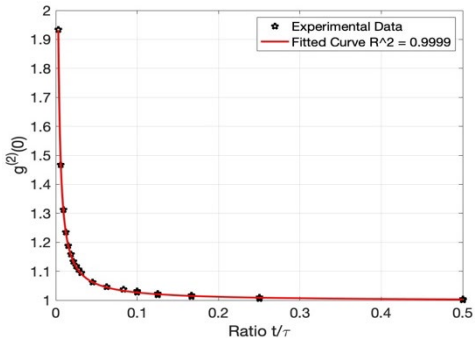

Figure 2. $\gamma^{(2)}(0)$ as a function of ratio t_c/τ_c . Dots represent the experimental data. Red curve represents the best fit function.

This figure indicates that a low ratio t_c/τ_c is necessary to reach the theoretical bunching of 2 for chaotic light sources.

In conclusion, the response time t_c exhibited a major impact on the experimental determination of $g^{(2)}(0)$, preventing the function to reach its theoretical maximum in some cases, and broadening its shape (temporal coherence τ_c). These effects can be modelled and eventually compensated by dedicated signal processing. These results can help to design and process signals more efficiently for ghost imaging, or any other intensity correlation-based imaging modality.

[1] Shapiro, J.H., Boyd, R.W. *Quantum Inf Process* **11**, 949 (2012).
[2] Y. Shih, *An Introduction to Quantum Optics*, CRC Press Taylor & Francis Group, (2018).

Acknowledgements: This work was supported by Ministerio de Ciencia e Innovación, Agencia Estatal de Investigación, Spain (PID2020-113919RB-I00).

Two lines of space reserved to include
codes of the symposium and of this communication

Characterization of topography hidden under paint by means of algorithms stable to the number of frames under non-uniform illumination

E. Baradit[1,*], M. Avendaño[2], G. Cañas[1], M. Yañez[3], M. Trivi[4], J. Cariñe[5]

[1]*Physics Department, Universidad del Bio-Bio, Av.Collao 1202, Concepción, Chile.*
[2]*Graduate student, Physics Department, Universidad del Bio-Bio, Av.Collao 1202, Concepción, Chile.*
[3]*Department of Statistics, Universidad del Bio-Bio, Av.Collao 1202, Concepción, Chile.*
[4]*Centro de Investigaciones Ópticas de La Plata, PO Box 3, Zip Code 1897, Argentina.*
[5]*Department of Electrical Engineering, Universidad Católica de la Santísima Concepción, Alonso de Ribera 2850, Concepción, Chile.*

*e-mail: ebaradit@ubiobio.cl

The ability to access information about topographies covered under some kind of layer and with a certain activity poses a current and interesting problem for science and technology. This topography is not visible in plain sight.

This study reviews the stability of different qualitative processing algorithms in relation to a processed number of frames N and under non-uniform illumination conditions for a sample covered in fresh paint in the process of drying. The sample consists of an aluminum tube (Fig.1) with perforations of different diameters and depths, illuminated with a 532 nm continuous laser, obtaining dynamic speckle images captured by a CMOS camera which were then processed [1].

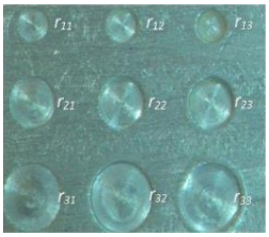

Figure 1: Photography of the sample with cylindrical perforations.

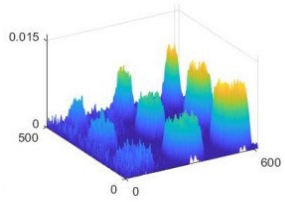

Figure 2: Mobility map obtained using NJDC algorithm.

The algorithms used were separated into non-normalized, including SF, MSF, STD, and DJC, and normalized, including Fujii, NSF, LSI, and NJDC. The NDJC is a modified normalized descriptor [2].

$$NDJC = \frac{1}{< I_k >^2} \sum_{k=1}^{N-1} \frac{(I_k - I_{k+1})^2}{I_k + I_{k+1}}$$

Figure 2 shows an example of mobility images obtained using this descriptor for N=250.

The results show that, under non-uniform illumination, the use of normalized qualitative descriptors to characterize topography hidden under paint reaches a high correlation (>0,98) and is stable to the number of frames (Fig. 3).

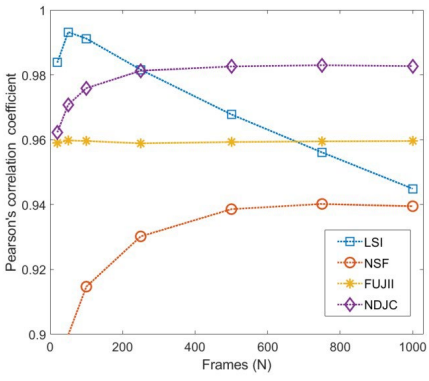

Figure 3: Correlation coefficients versus number of processed frames with normalized algorithms.

[1] Rabal H, Braga R., *Dynamic Laser Speckle and Applications.* CRC Press (2008).
[2] Cariñe J, Guzman R, Torres-Ruiz F., *Optics and Laser in Engineering* **82**, 56 (2016).

Two lines of space reserved to include
codes of the symposium and of this communication

Synchronous phase detection technique for the evaluation of complex functions displayed on a phase-only modulator

Esther Nabadda[1,*], Pascuala García-Martínez[2], María del Mar Sánchez-López[1,3], Ignacio Moreno[1,4]

[1]*Instituto de Bioingeniería, Universidad Miguel Hernández de Elche, 03202 Elche, Spain*

[2]*Departamento de Óptica y Optometría y Ciencias de la Visión, Universitat de València, 46100 Burjassot, Spain*

[3]*Departamento de Física Aplicada, Universidad Miguel Hernández de Elche, 03202 Elche, Spain*

[4]*Dept. Ciencia de Materiales, Óptica y Tec. Electrónica, Universidad Miguel Hernández de Elche, 03202 Elche, Spain*

*e-mail:enabadda@umh.es

In this work we combine an encoding method to display complex valued holograms onto a phase-only spatial light modulator (SLM) with a phase-shifting interferometric (PSI) technique for experimentally evaluating the generated complex valued optical fields. Increase in the potential applications of the so-called structured light has drawn great attention to this area of research. One key element is the liquid-crystal (LC) spatial light modulator (SLM) that, under illumination with linearly polarized light parallel to the LC director, produces a phase-only modulation. Using a 2D grating encoding technique [1], the SLM can be used to display complex valued diffractive elements. In most of the cases, the successful generation of the complex hologram is verified by regarding the light intensity distribution in the far field. In cases where the phase distribution is of interest, it is measured typically with a wave-front sensor or through an external interferometer that are added to the system generating the structured light, thus increasing the complexity of the setup.

Here, we demonstrate an efficient common-path polarization interferometer based on the SLM itself, not requiring any external additional element. The same setup can be used to simultaneously display the complex hologram and to apply the phase-shifting values required to retrieve the phase distribution. A simple rotation of a polarizer changes from the intensity configuration to the interferometer configuration. The continuous phase modulation provided by the SLM allows using arbitrary phase bias values, so different classical PSI algorithms [2] can be applied to recover the phase information. The figure shows different examples of the experimental realization of complex light beams based on the coaxial superposition of Laguerre-Gaussian beams. In each case the experimental intensity and phase distributions in the far field reproduce very well the theoretical results, thus confirming the validity of the technique.

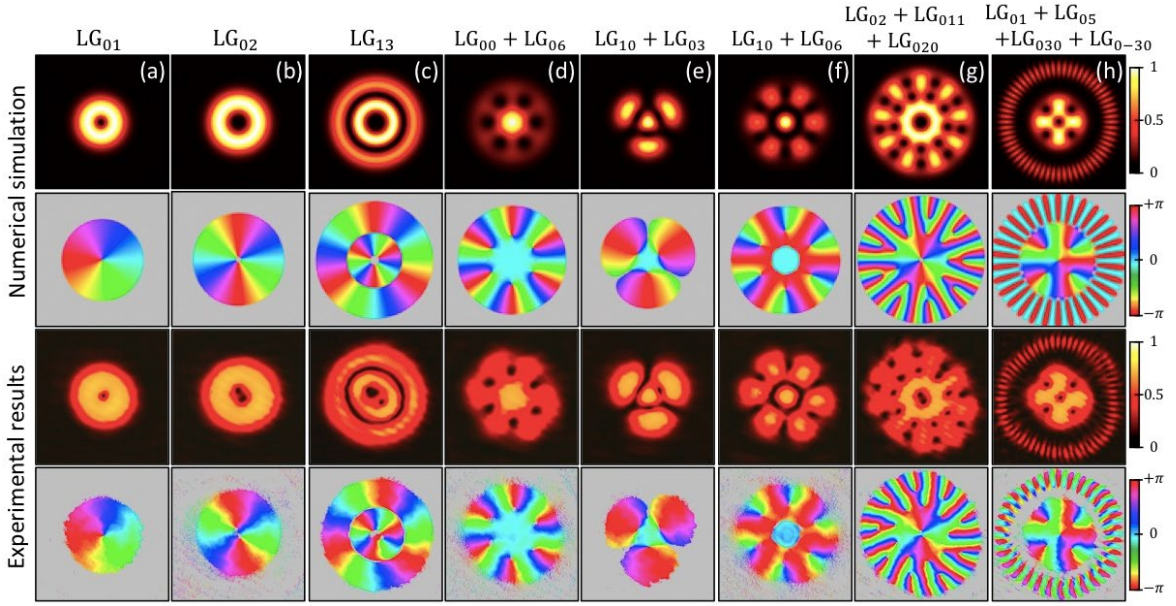

Figure 1. Realization of different superpositions of Laguerre-Gaussian beams. First and second row show simulations of the intensity and phase distributions. Third and fourth rows show the corresponding experimental results.

[1] J. A. Davis, E. D. Wolfe, I. Moreno, D. M. Cottrell, Encoding complex amplitude information onto phase-only diffractive optical elements using binary phase Nyquist gratings, *OSA Continuum* **4**(3), 896 (2021).

[2] K. Creath, Phase-measurement interferometry techniques, *Prog. Optics* **26**, 349 (1988).

Acknowledgements: This work received financial support from MICIN (grant project RTI2018-097107-B-C33). E.N. acknowledges a grant from GV (ref. GRISOLIAP/2020/004).

Two lines of space reserved to include
codes of the symposium and of this communication

Proof-of-concept depolarization emulator based on a liquid-crystal spatial light modulator

María del Mar Sánchez-López[1,*], David Marco[1], Guadalupe López-Morales[2], Ángel Lizana[3], Juan Campos[3], Ignacio Moreno[1]

[1]*Instituto de Bioingeniería, Universidad Miguel Hernández de Elche, Spain.*
[2]*Instituto de Investigación en Energías Renovables, Universidad de Ciencias y Artes de Chiapas, México.*
[3]*Departamento de Física, Universitat Autònoma de Barcelona, Spain.*

*e-mail: mar.sanchez@umh.es

There is an increasing interest in studying depolarization indices as channels to improve the image of biological samples [1]. Emulating depolarization effects with controlled precision can help to understand the depolarization mechanisms in these samples. In this work we demonstrate a proof-of-concept depolarization emulator that generates customized spatial patterns of the state of polarization (SoP) and degree of polarization (DoP). The technique is based on sequentially addressing two phase masks to a pixelated liquid-crystal spatial light modulator (SLM), in a time interval that is chosen to be the exposure time of our detector. The polarization properties of the output beam are verified by imaging the SLM screen onto a polarization camera and applying Mueller matrix imaging polarimetry, as shown in Fig. 1. The effective Mueller matrix of the SLM can be regarded as the averaged sum of two linear retarders with spatially-varying retardances $\phi_A(\mathbf{x})$ and $\phi_B(\mathbf{x})$, with $\mathbf{x}$=(x,y) being the spatial coordinates in the SLM. The effective SoP of the output beam is governed by the averaged retardance, while the DoP is governed by the retardance semi-difference $\overline{\delta(\mathbf{x})} = (\phi_A(\mathbf{x}) - \phi_B(\mathbf{x}))/2$. Further details are given in [2].

As an example, Fig.1 illustrates the two phase patterns sequentially addressed to the SLM encoding a word with gradually varying DoP. The phase value in some letters is indicated and the average retardance is $\bar{\phi} = 3\pi$ in all cases. The input state to the SLM is linearly polarized at 45º. Fig.1(c) shows on the Poincaré sphere (PS), and for each letter, the expected output states $\mathbf{S}_A$ (blue dots) and $\mathbf{S}_B$ (purple dots) generated by each pattern, and the theoretical averaged SoP (black dots). The averaged states lie all on the S_2 axis, with an effective DoP that changes gradually from one letter to the next according to $|\cos\bar{\delta}|$. For letters D and N the semi-difference phase is $\bar{\delta} = \pi/4$ and $\bar{\delta} = 3\pi/4$, hence their effective DoP is $\mathrm{DoP}_{\langle \mathbf{S}_e \rangle} = 1/\sqrt{2}$, while for letter R $\bar{\delta} = \pi/2$ and the output becomes fully depolarized. These results are confirmed experimentally by measuring the effective Stokes parameter S_2 and the effective DoP of the output beam, as shown in panels (d,e).

This technique could be useful in testing imaging polarimeters and in biomedical imaging.

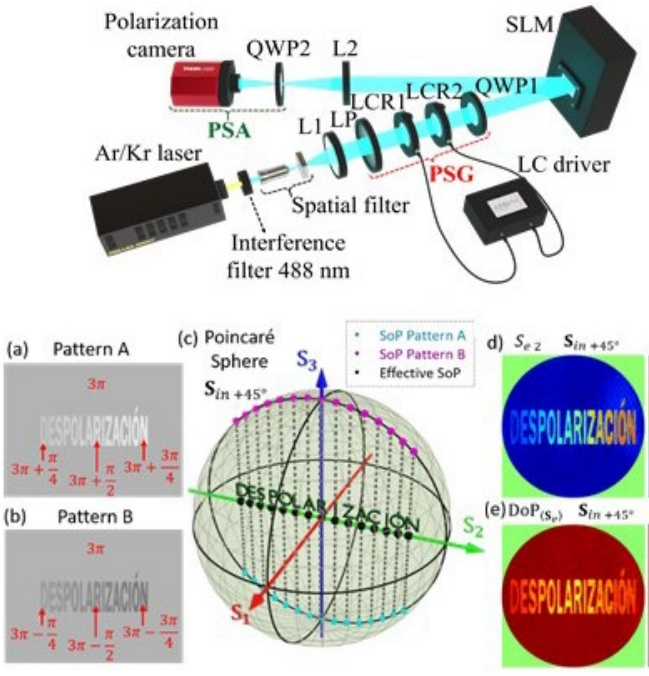

Figure 1. Scheme of the imaging Mueller polarimeter. (a,b) Phase patterns encoding a text, (c) theoretical Stokes parameters on the PS, (d,e) experimental effective Stokes parameter S_2 and DoP of the output beam.

[1] A. Lizana, A. Van Eeckhout, K. Adamczik, C. Rodriguez, J.C. Escalera, E. Garcia-Caurel, I. Moreno and J. Campos, *J. Biomed. Opt.* **22**, 056004 (2017).

[2] D. Marco, G. López-Morales, M.M. Sánchez-López, A. Lizana, I. Moreno and J. Campos, *Scientific Reports* **11**, 9415 (2021).

Acknowledgements: This work received financial support from MICIN (RTI2018-097107-B-C33 and –C31).

Two lines of space reserved to include
codes of the symposium and of this communication

Quality metrics in holographic lenses recorded in a low toxicity photopolymer

Tomás Lloret[1,2*], Víctor Navarro-Fuster[3], Marta Morales-Vidal[1], Manuel G. Ramírez[1], Kheloud Berramdane[1], José Carlos García-Vázquez[2], Inmaculada Pascual[1,2]

[1]*Instituto Universitario de Física Aplicada a las Ciencias y las Tecnologías, Universidad de Alicante, Carretera San Vicente del Raspeig s/n, 03690 San Vicente del Raspeig, España.*
[2]*Departamento de Óptica, Farmacología y Anatomía, Universidad de Alicante, Carretera San Vicente del Raspeig s/n, 03690 San Vicente del Raspeig, España.*
[3]*Departamento de Física, Ingeniería de Sistemas y Teoría de la Señal, Universidad de Alicante, Carretera San Vicente del Raspeig s/n, 03690 San Vicente del Raspeig, España*

*e-mail: tomas.lloret@ua.es

Holographic Lenses (HLs) are holograms obtained from the interference of an object point (object beam) and a plane beam (reference beam). Unlike conventional refractive lenses (RLs), their physical principle is diffraction, and in addition to spectral dependence, they also exhibit angular dependence [1]. One of the main applications of such HLs is their use in AR optical systems such as head mounted displays (HMD).

HLs also exhibit aberrations [2]. To measure the impact of these aberrations, diffraction efficiency is not a suitable optical parameter. For this purpose, different quality metrics can be used. In this work, the quality of positive symmetrical and negative asymmetrical HLs has been evaluated by studying different metrics: optical quality metrics (Zernike and Seidel coefficients, RMS for Zernike and Seidel aberrations, and critical pupil fraction (PF)); and image quality metrics based on the impulse response of the system (Strehl Ratio (SR), Entropy and cut-off frequency) [3]. The results obtained can be seen in Table 1.

	Positive Symmetrical HLs					Negative Asymmetrical HLs				
Zernike Coef. (μm)	C_4^0	C_2^{-1}	C_3^1	C_2^{-2}	C_2^2	C_4^0	C_2^{-1}	C_3^1	C_2^{-2}	C_2^2
	$-9 \cdot 10^{-3}$	$1.1 \cdot 10^{-1}$	$-2.2 \cdot 10^{-2}$	$-1.8 \cdot 10^{-1}$	0	$-6 \cdot 10^{-3}$	$2.3 \cdot 10^{-2}$	$-6 \cdot 10^{-3}$	$-1.5 \cdot 10^{-6}$	$-7 \cdot 10^{-6}$
Seidel Coef. (μm)	S		C		A	S		C		A
	$8.05 \cdot 10^{-5}$		$2.21 \cdot 10^{-3}$		$6.06 \cdot 10^{-2}$	$-8.05 \cdot 10^{-5}$		$-1.94 \cdot 10^{-5}$		$3.01 \cdot 10^{-7}$
RMS Zernike (μm)	0.209					0.030				
RMS Seidel (μm)	0.011					$1.56 \cdot 10^{-5}$				
PF	0.063					0.25				
SR	0.124 (~12%)					0.856 (~86%)				
Normalized Entropy (10^{-3})	7.7					1.7				
Theoretical Cutoff Freq. (cycles/degree)	68.2					110.7				

Table 1. Optical and image quality metrics for positive symmetrical and negative asymmetrical HLs.

The best results were obtained for negative asymmetrical HLs, therefore their geometry is the most suitable for optical imaging systems.

[1] T. Lloret, V. Navarro-Fuster, M.G. Ramírez, M. Ortuño, C. Neipp, A. Beléndez, and I. Pascual, Holographic Lenses in an Environment-Friendly Photopolymer, *Polymers* **10** (3), 302 (2018).
[3] T. Lloret, V. Navarro-Fuster, M.G. Ramírez, M. Morales-Vidal, A. Beléndez, and I. Pascual, Aberration-Based Quality Metrics in Holographic Lenses, *Polymers* **12** (4), 993 (2020).
[2] P. Artal, *Handbook of Visual Optics* Vol. II (CRC Press, Abingdon UK, 2017).

Acknowledgements: This research was funded by Ministerio de Ciencia, Innovación y Universidades, Spain, under project PID2019-106601RB-I00; Generalitat Valenciana, Spain, under projects CDEIGENT/2018/024, PROMETEO/2021/006, and IDIFEDER/2021/014 (co-funded by European Union through the FEDER Programme); Universidad de Alicante, Spain, under UAFPU20-23.

Reflection gratings stored in a nanoparticle-doped photopolymer

José Carlos García-Vázquez[1,*], Manuel G. Ramírez[2], Kheloud Berramdane[2], José Solla-Gullón[3], Marta Morales-Vidal[2], Tomás Lloret[1] and Inmaculada Pascual[1,2]

[1] *Departamento de Óptica, Farmacología y Anatomía, Universidad de Alicante,Carretera San Vicente del Raspeig s/n, 03690 San Vicente del Raspeig, Spain.* [2] *I.U. Física Aplicada a las Ciencias y las Tecnologías Universidad de Alicante, Ap.99, Alicante E-03080.* [3] *Instituto de Electroquímica, Universidad de Alicante, Ap.99, Alicante E-03080, Spain.*
*e-mail: jcgv5@alu.ua.es

Nowadays, the study and optimization of volume holography reflection gratings stored in environmentally compatible photopolymers has a great interest since they can be used as holographic optical elements. One of the main advantages of reflection holograms is that they can be reconstructed using white light. This allows to develop holographic sensors [1]. Unslanted reflection holograms have been stored in an acrylate-poly(vinyl alcohol) based photopolymer development in our research group [2]. With the main objective of increasing the diffraction efficiency of reflection holograms, a series of chemical modifications have been introduced in the same acrylated-based photopolymer. Specifically, this material has been doped with Platinum nanoparticles (Pt-NP), increasing the refractive index modulation in the recorded diffraction gratings. A solid-state laser emitting at 455 nm was employed for stored the unslanted reflection gratings at high spatial frequencies.

Figure 1 shows the transmittance as a function of reconstruction wavelength for doped and undoped photopolymer films. The increase in diffraction effciency is clearly observed when the photopolymer is doped with Pt nanoparticles compared to the value obtained for the undoped photopolymer. A blue-shift wavelength for maximum diffraction effciency is observed in the Pt doped grating. The experimental values are fitted according to Kogelnik's Coupled Wave Theory [3] in order to obtain the optical parameters that described the reflection gratings. Doping with the Pt-NP nanoparticles produces a change in the average refractive index that gives rise to the blue-shift wavelength and an increase in the refractive index modulation that produces a greater diffraction efficiency.

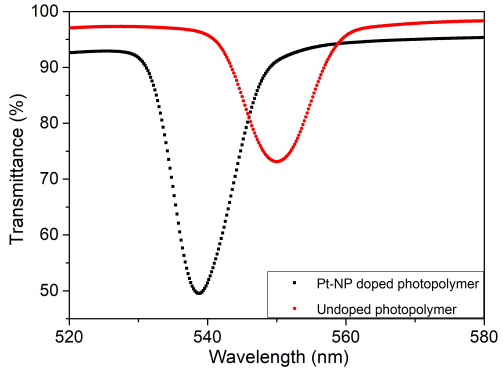

Figure 1: Transmittance as a funtion of reconstruction wavelength for a Pt doped grating (black) and an undoped grating (red).

[1] Yetisen, A. K., Naydenova, I., da Cruz Vasconcellos, F., Blyth, J., Lowe, C. R. . Holographic Sensors: Three-Dimensional Analyte-Sensitive Nanostructures and Their Applications. Chemical Reviews, 114, 10654-10696 (2014).

[2] Ramírez, M. G., Sirvent, D., Morales-Vidal, M., Ortuño, M., Martínez-Guardiola, F., Francés, J., Pascual, I. LED-Cured Reflection Gratings Stored in an Acrylate-Based Photopolymer. Polymers, 11, 632 (2019).

[3] Kogelnik, H. Coupled Wave Theory for Thick Hologram Gratings. *The Bell System Technical Journal*, 48, 2909-2948 (1969).

Funding: This research was funded by Ministerio de Ciencia, Innovación y Universidades, Spain, under project PID2019-106601RB-I00; Generalitat Valenciana, Spain, under projects CDEI-GENT/2018/024, PROMETEO/2021/006, and IDIFEDER/2021/014 (co-funded by European Union through the FEDER Programme).

Two lines of space reserved to include
codes of the symposium and of this communication

Redes plasmónicas unidimensionales de nanopartículas de oro a partir de redes de relieve fabricadas holográficamente

Jose C. Mira-Martínez[1,*], Víctor Bonal[1], José A. Quintana[2], José M. Villalvilla[1], Pedro G. Boj[2], María A. Díaz-García[1]

[1]*Departamento de Física Aplicada, Universidad de Alicante, 03080 Alicante, España.*
[2]*Departamento de Óptica, Farmacología y Anatomía, Universidad de Alicante, 03080 Alicante, España.*

*e-mail: carlos.mira@ua.es

En los últimos años, las nanopartículas de oro han logrado captar la atención en el campo de la fotónica debido a sus diversas propiedades ópticas. La resonancia del plasmón superficial permite realizar medidas cuantitativas de procesos superficiales, particularmente útil en el desarrollo de sensores de película delgada, de una manera simple y con alta sensibilidad.

Las estructuras fotónicas basadas en nanopartículas metálicas son buenas candidatas en la aplicación de nanodispositivos ópticos debido a su interacción con la luz. Entre sus diversas propiedades, pueden destacarse el guiado de luz a escala nanoscópica o una fuerte amplificación del campo en volúmenes muy pequeños. Existen diferentes estructuras posibles, siendo las redes unidimensionales formadas por nanopartículas metálicas una de las más estudiadas en los últimos años.

En este trabajo se presenta un método novedoso de fabricación de redes plasmónicas unidimensionales de nanopartículas de oro, que pueden tener espaciados de red (periodo) de tan solo 200 nm. El método se basa en un procedimiento desarrollado en nuestro grupo de investigación para la fabricación de redes de relieve en gelatina dicromatada (DCG), consistente en el uso de litografía holográfica y posterior revelado en un plasma de oxígeno [1]. Para la obtención de las nanopartículas de oro se utiliza $HAuCl_4$ como precursor, añadido en una de las etapas del anterior proceso, utilizando además tratamientos térmicos posteriores controlados para favorecer la nucleación.

La formación de nanopartículas fue monitorizada a través de espectroscopia de absorción en diferentes partes del proceso (ver Figura 1). Por otro lado, la distribución de las nanopartículas de Au en función de los parámetros del proceso se estudió mediante imágenes de electrones retrodispersados de microscopía electrónica de barrido (SEM), Figura 2.

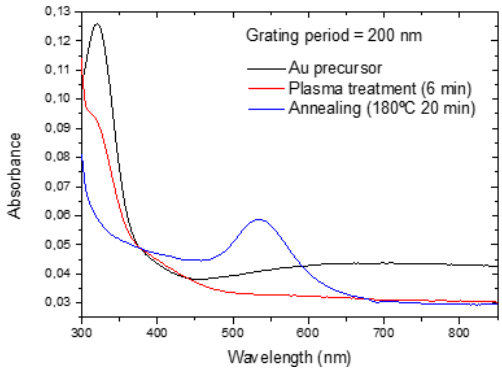

Figura 1. Espectro de absorción de una muestra al introducir el precursor de oro (línea negra), tratamiento de plasma (línea roja) y tratamiento térmico a 180ºC durante 20 min (línea azul).

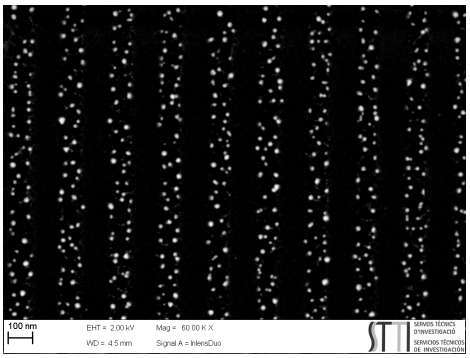

Figure 2. Imagen de BS-FESEM de una red de 200 nm tras un tratamiento en plasma de oxígeno durante 3 min y un tratamiento térmico de 120ºC durante 8 horas.

[1] J. A. Quintana et al., *Optical Mater* **5**, 1700238 (2017).

Two lines of space reserved to include
codes of the symposium and of this communication

Latest advances in organic distributed feedback lasers with top-layer resonators

V. Bonal[1,*], J. A. Quintana[2], J. M. Villalvilla[1], P. G. Boj[2],
R. Muñoz-Mármol[1], J. C. Mira-Martínez[1], M. A. Díaz-García[1]

[1]*Departamento de Física Aplicada, Instituto Universitario de Materiales de Alicante, Universidad de Alicante, 03080 Alicante, Spain.* [2]*Departamento de Óptica, Farmacología y Anatomía, Instituto Universitario de Materiales de Alicante, Universidad de Alicante, 03080 Alicante, Spain.*

*e-mail: victor.bonal@ua.es

Distributed feedback lasers (DFB) are some of the most studied thin film organic lasers, as they are cost-efficient, compact, and easily integrated with other devices. This allows them to be used for a wide range of applications, such as spectroscopy, optical communications, and sensing [1]. DFB lasers typically consist in an active material thin film deposited over a grating engraved in an inorganic substrate. However, DFB lasers can present different architectures depending on the position of the resonator and the materials used for its fabrication.

Here, we study a different DFB architecture with a polymeric resonator deposited on top of the active film [2]. This architecture offers several advantages over the standard one. The device is easier to fabricate, as both films are organic and solution-processable. Additionally, the active film presents a uniform thickness, and the grating period can be easily adjusted for each case as it is fabricated using holographic lithography. In this work, we are going to focus on the influence of the different grating parameters on the final device characteristics, in order to optimize the threshold and efficiency of the devices [3]. Additionally, we are going to explore the capabilities of this architecture to fabricate deep-blue-emitting lasers [4] and we to compare these devices with the standard configuration ones to further explore the advantages of this architecture and the differences between them [5].

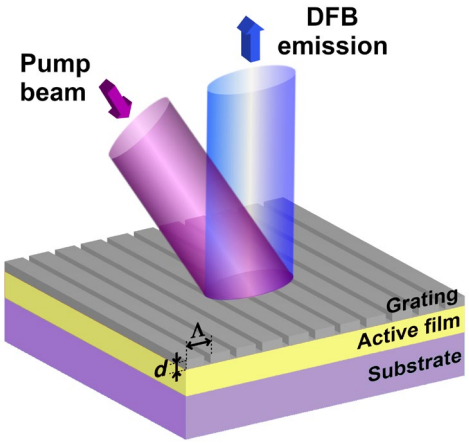

Figure 1. Scheme of the DFB device architecture, including pumping and collection geometry (Λ: grating period; d: grating depth).

[1] Kuehne, A. J. C. & Gather, M. C., *Chem. Rev.* **116**, 12823 (2016).
[2] Quintana, J. A. *et al.*, *Adv. Opt. Mater.* **5**, 1700238 (2017).
[3] Bonal, V., Quintana, J. A., Villalvilla, J. M., Boj, P. G. & Díaz-García, M. A., *Sci. Rep.* **9**, 11159 (2019).
[4] Bonal, V. *et al.*, *Adv. Opt. Mater.* **8**, 2001153 (2020).
[5] Bonal, V. *et al.*, *Polymers* **13**, 3843 (2021).

Acknowledgements: Funding from Spanish Ministry of Science and Innovation (grant no. PID2020-119124RB-I00) and Conselleria de Innovación, Universidades, Ciencia y Sociedad Digital de la Comunidad Valenciana (grant no. AICO/2021/093). We also thank V. Esteve and I. Garcés for technical assistance.